European Southern Observatory
Organisation Européenne pour des Recherches Astronomiques dans l'Hémisphère Austral
Europäische Organisation für astronomische Forschung in der südlichen Hemisphäre

VLT PROGRAMME

Very Large Telescope

FORS:
An assessment of obtainable photometric accuracy and outline of strategy for improvement

P. Møller, A. Järvinen, G. Rupprecht, W. Freudling, F. Patat, M. Romaniello,

M. E. van den Ancker, M. G. Petr-Gotzens, E. Jehin, R. Mignani, K. O'Brien, T. Szeifert

(FORS IOT Secondary Standards Working Group)

VLT-TRE-ESO-13100-3808

Issue: 1.

Issue date: 17.11.2005

Prepared: P. Møller et al. .....
Name Date Signature

VLT PROGRAMME ⋆ Telephone: +49-89-32006-0 ⋆ Fax: +49-89-3202362

CHANGE RECORD

ISSUE	DATE	SECTION/PAGE AFFECTED	REASONS/INITIATION DOCUMENTS/REMARKS
1.	17.11.2005	all	new document

Contents

List of Figures

This page intentionally left blank

1 Scope and Executive Summary

1.1 Scope

The FORS Secondary Standard Working Group (FSSWG) is a cross–division group reporting to the FORS IOT. It was formed following the resolution of action item AI03-5 (see Appendix A), and was charged with exploring ways of optimizing the photometric calibration of FORS and with assessing the possibility to carry out a project to define photometric standards for current and future large aperture optical telescopes. This is the final report of the FSSWG. A related project to FSSWG is the FORS Absolute Photometry project (FAP) which will build on the results of the current findings to investigate the accuracy of absolute photometry achievable with FORS. That project has already collected data which are currently being analyzed.
In this report we first (Sect. 2–3) detail the problems inherent in obtaining CCD images with no zero-point variation across the field and describe possible methods to avoid, control and/or remove them (Sect. 4).
We develop the necessary algorithmic tools (Sect. 5), and apply those (Sect. 6) to a large number of simulated CCD data where we throw a number of realistic problems into the simulated data in order to explore how well the code responds. This provides us with a set of scaling relations which are useful for defining optimal observing strategies and for predicting obtainable accuracies.
We then apply our tools to two sets of test data (one in R band one in B band) obtained with FORS1 (complete observing log in Appendix B), and report the results in Sect. 7.

1.2 Executive Summary

Our main results are the following:

- We find that the current calibration strategy for FORS provides a photometric calibration which at its worst gives a 0.06 magnitude variation (i.e. ± 0.03 systematic variation) across the field. For the largest part of the field it is only ± 0.02 magnitude. This is well within the guaranteed accuracy of 10%, but it is not accurate enough for the purposes of a Secondary Standard Project.
- We find that our observing strategy, together with our algorithm to improve relative photometry, is accurate enough to carry out a project to define a set of secondary standard fields. However, secondary standards based on the Landolt fields cannot directly be obtained with FORS because the shutter timing uncertainties will dominate the photometric errors for the very short exposure times needed. The project would therefore have to be carried out, at least partly, on a smaller telescope.

In Sect. 8.8 we present our immediate recommendations which are briefly summarized here:

- We recommend to review the current standard calibration strategy for FORS imaging. We propose two strategies both of which should improve

the relative photometry, and both of which may even be simpler than the current. The feasibility and relative merit of the two procedures will be further investigated in FAP.

- We present a possible plan for reverse engineering of the process which should improve the calibration also of archival FORS data.
- We point out that the algorithmic method we have developed is not restricted to only work for FORS data, but that the issue of across field zero-point variation is a global issue which only recently has come to the attention of a larger community. It may be worth in the longer terms to consider how our experience from this project may be transferred to other instruments, possibly one could consider to incorporate our algorithm into the framework of the ESO CPL.
- Secondary standards for 8m-class telescopes are being collected by at least two independent groups. The absolute photometric accuracy with FORS achievable using those standards is currently being investigated by FAP. We recommend to base the decision to start to collect data for ESO secondary photometric standards on the outcome of that project.
- The Danish 1.5m is still available to ESO 6 months per year for no cost other than running it. This could be a possible option for obtaining secondary standards.

2 Introduction

The problem of accurate photometric calibration of imaging data from 8 meter class telescopes is a long standing issue. It arises from the fact that primary high precision photometric standard stars were defined in an era of much smaller apertures, and therefore are much too bright for efficient use at large telescopes. Many bright standards can be observed only in very short exposures (less than one second), which causes the shutter time error to become significant [1]. The problem was recognized early in the history of VLT operations, and several steps have been taken to address it. Already during Period 63 it was decided always to observe standard star fields twice, a long and a short exposure. The plan, in the long run, being that the long exposures could form the basis of a project to define a set of secondary standards. This plan, however, neglected the potential problem inherent in CCD field photometry, that the zero point often varies across the field (there are several reasons for this - for details see Sect. 3 below).

The FORS IOT decided to investigate possible solutions to the problem (FORS-IOT action item AI03-5) and a report and proposal was presented to the FORS IOT (Møller, 2003; see Appendix A). Based on this the FORS Secondary Standard Working Group (FSSWG, popularly known as the Fizz-wig) was formed and a first FORS test run defined and carried out. The first Fizz-wig report (Järvinen *et al.*, 2005; reproduced in Appendix E for easy reference) deals with

[1] Another potential problem with calibration of short exposures is atmospheric scintillation effects. This turns out not to be a significant source of errors for FORS (see Appendix D)

FORS bias subtraction, bad pixels and variability of twilight sky images. One important conclusion of that report is that R band twilight sky images (often referred to as "SKYFLATS") vary (on the night of our observations) by 0.8% on a timescale of minutes, and by 3% compared to a similar run a year later.
Two technical memos related to the work of FSSWG deal in more detail with specific issues raised in Report I: *(i)* The twilight sky images (Mignani and Petr–Gotzens, 2005) and *(ii)* the issue of shutter time effects (Patat & Romaniello, 2005). The results of the Mignani and Petr–Gotzens report on sky-flats are discussed in detail in Appendix C but can briefly be summarised as follows: The twilight sky-flats show erratic variations of up to 5% across the field of FORS, causing the photometric zero-point to vary with 0.05 magnitude across the field. The strongest variations are seen in the corners of the CCD, and we interpret this to be instrumental. Patat (2003) performed a related test on 4678 reduced FORS1 frames obtained between April 1, 2000 and September 30, 2001. The conclusion from that paper was (Fig. 10 in that paper) that sky values mostly cluster around 1.5-2% away from the mean, but that there is a tail stretching out to a bit more than 3% (absolute). This implies a peak-to-peak of around 6%, similar to the result above.
Following up on the indications, found independently in those three reports, we downloaded all U, B, V, R and I band sky-flats taken between Jan 1st and Sept 30, 2005, a total of 293 images and produced streaming time-sequences for each band. In the time-sequences we also included a marker to identify the rotator angle. Simply viewing the time sequences firstly confirms the erratic behaviour of the images, but in addition it is also seen that there are clearly visible features that follow the rotation of the field. This indicates that indeed at least part of the variation is caused by the rotation of the instrument, either by vignetting or by reflections inside the instrument. Viewing the time sequence also reveals that non-flatfieldable features exist on many different scales, including small scales.
A proposal for a second FORS run of photometric tests, based on preliminary results of the current work, was submitted and approved: The FORS Absolute Photometry project (FAP) (Freudling *et al.*, 2005).

The aims of this report are to present recommendations for: *(i)* How to obtain the best photometric calibration capability of FORS in the future. *(ii)* How to optimize the photometric calibration of past FORS data. *(iii)* How to create secondary photometric standard fields suitable for current and future large aperture optical telescopes.

3 Decomposing twilight sky images

One of the most basic, and most important, steps in the reduction of CCD imaging data is the correction of the "total instrument efficiency" at the position of each pixel. This is often referred to as "flat-fielding", a term taken from the common practice of obtaining images of a large illuminated area (e.g. an illuminated screen or the twilight sky), and then interpret a suitably summed and normalized combination of those as the (x, y) efficiency map.

In cases where no high accuracy of relative photometry across the field is needed, the "twilight flat" procedure is sufficient and has the advantage of being both fast and simple. However, when higher accuracy is needed this method fails. The reason it fails is that it rests upon two implicit, but incorrect, assumptions. It assumes that *i)* the twilight sky is evenly illuminated, and *ii)* all photons that enter the telescope arrive on the CCD in focus. As we have seen from the discussion of the "SKYFLATS" in Sect. 2, neither of the two assumptions are in general correct. The twilight sky has a gradient which can be computed (Schaefer, 1998) as shown in Fig. 1, and from which we can predict that the gradient across the FORS field at most should be 0.9%. An empirical study (Chromey & Hasselbacher, 1996) gives the same result.

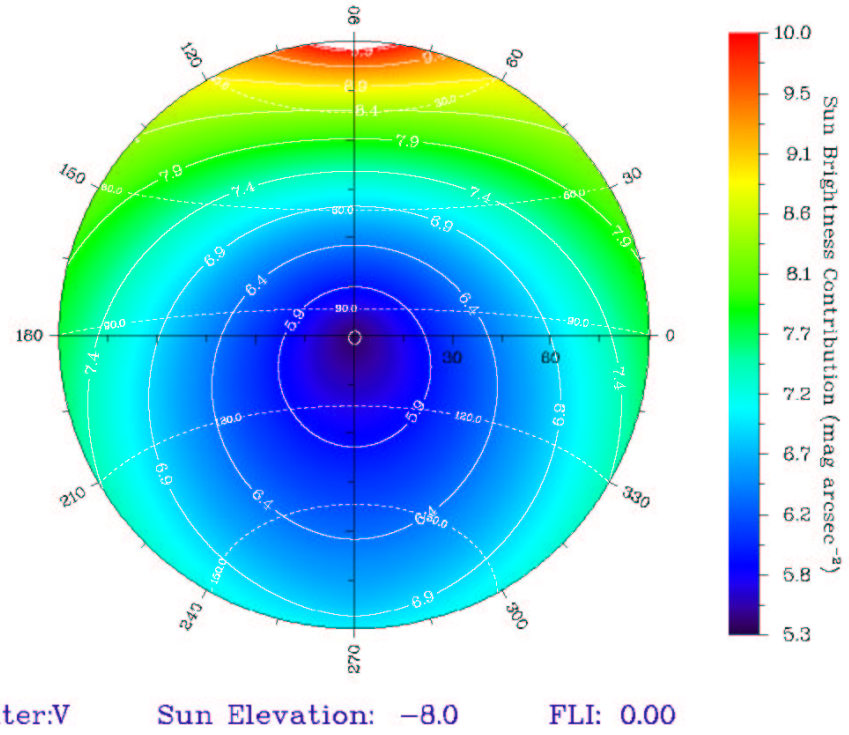

Figure 1:

Because the term "flat-field" has an imprecise definition (as described above), we shall in the remainder of this document attempt to avoid the use of it entirely. We shall refer to an image obtained during twilight as a "twilight sky image" ($TSI(x, y)$), and a frame which is meant to correct a nighttime exposure such that all pixels have the same photometric zero-point for the photons that arrived on the CCD in focus, we shall refer to as a "quantum efficiency frame" ($QEF(x, y)$).

To conclude from above: The twilight sky is not an evenly illuminated screen, it has a large scale gradient. In addition, when a telescope is pointed to the twilight sky only a part of the photons will follow the intended optical path through telescope and instrument to produce a correct, focused, representation of the sky on the CCD, while the remaining photons will follow different optical paths and may end up in an unfocused image superimposed on the sky image.

In a focal reducer type instrument, such as FORS, this unfocused image can conveniently be though of as the sum of two components: *i)* The many optical surfaces all reflect part of the photons, and after multiple reflections some of the photons hit the CCD in a characteristic pattern concentrated towards the centre of the field and with falling intensity towards the edges. This produces a smooth, large scale, often rotationally symmetric "hump" which is aptly known as "central light concentration". In most instruments part of the optical surfaces have been tilted at a small angle in order prevent reflection ghosts in the field, thereby also altering the central light concentration pattern. *ii)* Photons can scatter off any other surface inside the instrument. If they scatter off moving parts (e.g. the guide probe) they can produce highly variable and non-symmetric patterns. Because those patterns also are made from unfocused images, they will be smooth on some scale, but the scale could be smaller than that of both sky gradient and light concentration.
We can now simply describe the twilight observation as:

$$TSI(x,y) = F(x,y) \cdot QEF(x,y) \tag{1}$$

where $F(x,y)$ is the sum of sky, central light concentration, and the variably scattered component. Our goal is to determine $QEF(x,y)$ to the best possible precision and, since $TSI(x,y)$ is an observable, our task is therefore reduced to that of determining $F(x,y)$. It is important here to note that the only thing which is constant in Equ. (1) is $QEF(x,y)$. For each new observation of the twilight sky one will obtain a new and different $TSI(x,y)$, and consequently also the "correction frame" $F(x,y)$ will have changed.

4 Strategies for determination of $F(x,y)$

Because $F(x,y)$ consists only of components that are smooth on scales much larger than several pixels, we only need to determine it in N points distributed around the field, and then either interpolate between those points or fit a 2D surface to them. The value of N is set by the smallest scales on which we expect $F(x,y)$ to have significant power. For the sky gradient the typical scale is that of the sky, i.e. much larger than the field, while instrumental effects may be on almost any scale.

4.1 Single star dither strategy

A simple way to visualize this process is to choose a constant light source (e.g. a non-variable star), take N images where that same star is placed on N different positions on the CCD. When we divide those images by $TSI(x,y)$ then we correct for the pixel efficiencies, $QEF(x,y)$, but at the same time we introduce a large scale error field $F(x,y)$. Because the star in non-variable, the variation of its brightness across the field will reflect exactly $F(x,y)$ which can then be determined by the fitting of a surface to the N values. In practice this strategy may be a little hard to employ as it requires highly photometric observing conditions. Also, if N is large (e.g. 100 exposures for a 10 by 10 grid), then the exposures will be taken at different airmass which needs to be corrected for.

4.2 Dither field strategy

A more efficient method is to choose a field with many stars, rather than a single star, usable for accurate photometric measurements. Obtaining many dithered images of such a field will place many stars on different parts of the CCD, and they will combine to provide redundant information for determination of $F(x, y)$, relative zero-points of all images, and instrumental magnitudes of all stars. This makes it possible to determine the photometric correction field even under non-photometric conditions.
One thing is important to keep in mind. Specific types of off-sets are invariant for specific symmetries, and therefore cannot be used to determine all components of the correction. Rotations of the field, for instance, are unable to recognize any components with rotational symmetry and therefore cannot correct those. Linear offsetting will take out rotational symmetries, but is not able to recognize any linear terms in the correction. More precisely, with only linear offsets one cannot tell the difference between a linear correction term, and a difference in zero-point. This turns out to be very important for the implementation of a code, because errors in zero-points turn out to be the dominating error source in the fitting procedure (see also Andersen, Freyhammer and Storm, 1995). Correction schemes of the type described above have already been applied to WFI data (Koch, Odenkirchen, Grebel, and Caldwell, 2003; Vandame, 2004).

4.3 First test implementation

Following the above considerations we decided for a first test to use an 8-frame dither/rotation combination:

- Starting with an exposure of the central field we rotated 90, 180, and 270 degrees. We then off-setted half a field size in the four diagonal directions NE, NW, SE, and SW relative to central field (see Fig. 2).

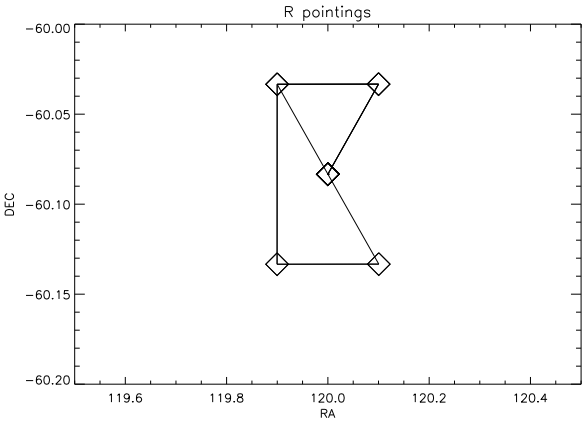

Figure 2: FORS test run off-set pattern

The basic reduction of those data was discussed in detail in Report I, and the final results will be presented here (Sect. 7.2). First, we will now describe and test the algorithm we are going to use to determine $F(x, y)$.

5 Algorithm for determination of $F(x, y)$

5.1 Description of the algorithm

The instrumental magnitudes measured on a single image obviously do not contain any information on $F(x, y)$. If a second image offset by a fraction of the image size is taken under identical conditions, each pair of instrumental magnitudes of the same star on both images contains information on the difference in throughput between the two position on the detector. However, unless images are taken under photometry conditions, this information is modulated by the difference in the magnitude zero points of the two images. With a sufficient number of dithered images, several pairs of stars can be used to simultaneously fit the relative zero points between any two images and the parameters of a model for $F(x, y)$.
In general, each measured magnitude on any of the images can be written as

$$m_{\nu\mu} = M_\nu + z_\mu - f(x, y) \tag{2}$$

where M_ν is the magnitude of star ν within the chosen band, $m_{\nu\mu}$ is its instrumental magnitude measured on image μ, and z_μ is the zero point of image μ. The quantity $f(x, y)$ is $F(x, y)$ expressed in magnitudes, i.e.

$$f(x, y) = -2.5 \log F(x, y) \tag{3}$$

The specific model for $f(x, y)$ we used for the fit to the current data set is a polynomial of order o,

$$f(x, y) = \sum_{i=0}^{o} \sum_{j=0}^{o-i} p_{ij} x^i y^j. \tag{4}$$

The magnitude for the $n+1$ different observed stars, M_ν where $\nu = 0 \ldots n$, and the zero points of the $m+1$ different images, z_μ, $\mu = 0 \ldots m$, are further free parameters. Two of the three parameters $p_{0,0}$, M_0 and z_0 are redundant and can be arbitrarily fixed. Choosing $M_0 = z_0 = 0$, the full set of equations 4 can be written as

$$\mathbf{A} \cdot \mathbf{p} = \mathbf{M} \tag{5}$$

where $\mathbf{p}$ is the parameter vector

$$\mathbf{p} = \begin{pmatrix} p_{0,0} \\ p_{1,0} \\ p_{0,1} \\ \vdots \\ p_{kl} \\ M_1 \\ M_2 \\ \vdots \\ M_n \\ z_1 \\ z_0 \\ \vdots \\ z_m \end{pmatrix} \tag{6}$$

$\mathbf{M}$ is the vector of measured instrumental magnitudes,

$$\mathbf{M} = \begin{pmatrix} m_{0,0} \\ m_{1,0} \\ m_{2,0} \\ \vdots \\ m_{n,0} \\ m_{0,1} \\ m_{1,1} \\ \vdots \\ m_{n,m} \end{pmatrix} \tag{7}$$

and the matrix $\mathbf{A}$ is

$$\mathbf{A} = \begin{array}{r} \\ 0 \\ 1 \\ 2 \\ \vdots \\ n \\ n+1 \\ n+2 \\ \vdots \\ n \times m \end{array} \begin{array}{c} \begin{array}{cccccccccccc} p_{0,0} & p_{1,0} & p_{0,1} & \cdots & p_{kl} & M_1 & M_2 & \cdots & M_n & z_1 & z_2 & \cdots & z_m \end{array} \\ \begin{pmatrix} 1 & x_0 & y_0 & \cdots & x_0^k y_0^l & 0 & 0 & \cdots & 0 & 0 & 0 & \cdots & 0 \\ 1 & x_1 & y_1 & \cdots & x_1^k y_1^l & 1 & 0 & \cdots & 0 & 0 & 0 & \cdots & 0 \\ 1 & x_2 & y_2 & \cdots & x_2^k y_2^l & 0 & 1 & \cdots & 0 & 0 & 0 & \cdots & 0 \\ & \vdots & & & & \vdots & & & & & \vdots & & \\ 1 & x_n & y_n & \cdots & x_n^k y_n^l & 0 & 0 & \cdots & 1 & 0 & 0 & \cdots & 0 \\ 1 & x_0 & y_0 & \cdots & x_0^k y_0^l & 0 & 0 & \cdots & 0 & 1 & 0 & \cdots & 0 \\ 1 & x_0 & y_0 & \cdots & x_0^k y_0^l & 1 & 0 & \cdots & 0 & 1 & 0 & \cdots & 0 \\ & \vdots & & & & \vdots & & & & & \vdots & & \\ 1 & x_0 & y_0 & \cdots & x_0^k y_0^l & 0 & 0 & \cdots & 1 & 0 & 0 & \cdots & 1 \end{pmatrix} \end{array} \tag{8}$$

The parameters corresponding to each column are shown on the top of the matrix. Note that only a subset of all stars is contained in any single image, the

labeling of the rows on the left side of the matrix is therefore not necessarily consecutive. The total number of free parameters to be determined n_p is

$$n_p = n + m + \sum_{i=0}^{o}(i+1) = n + m + \frac{o^2 + 3o + 2}{2} \tag{9}$$

whereas the number of equations is identical to the number of measured instrumental magnitudes. If the number of instrumental magnitudes per image is $>> 2$, then Equ. (5) is an over-determined set of linear equations.
Singular Value Decomposition (SVD) can be used to find the unknown zero-points, magnitudes and model parameters simultaneously in a least-square sense. SVD works by decomposing the matrix $\mathbf{A}$ into a square diagonal matrix $\mathbf{w}$ with positive or zero elements, and two orthogonal matrices $\mathbf{u}$ and $\mathbf{v}$,

$$\mathbf{A} = \mathbf{u} \cdot \mathbf{w} \cdot \mathbf{w^t}. \tag{10}$$

Then the least square solution for $\mathbf{M}$ can be found as

$$\mathbf{p} = \mathbf{v} \cdot \mathbf{w'} \cdot \mathbf{u^t} \cdot \mathbf{M} \tag{11}$$

where $\mathbf{w'}$ is a matrix which consists of a the inverse of a $n_p \times n_p$ submatrix of $\mathbf{w}$ and is set to zero elsewhere (see Press et. al. for details).
One consideration for solving this set of equations is to assign proper weights to each equation. Equ. (5) still holds when each row in the matrix $\mathbf{A}$ as well as corresponding elements of the vector of instrumental magnitudes are multiplied by an arbitrary weight. We weighted each equation taking into account both the uncertainty in the measured instrumental magnitudes and the local density of stars.
The estimated uncertainty $\sigma_{\nu\mu}$ in the instrumental magnitude of the ν^{th} star in the μ^{th} field as given by DAOPHOT were used to compute a weight w_m,

$$w_m = \frac{1}{\sigma^2_{\nu\mu}} \tag{12}$$

A significant source of uncertainty in the fit of our model to the zero points is the difference between the true shape of $f(x, y)$ and that of the model polynomial. If an unweighted fit of a polynomial were used, more weight would be given to regions with high density of observed stars. This would introduce biases in the fit which can be avoided by adjusting the weights according to the local density of stars. Specifically, we have used the inverse of the local density of w_m to compute a second weight w_ρ,

$$w_\rho = \frac{1}{\sum w_m} \tag{13}$$

where the sum in this equation is taken over all magnitude measurements in cells of 128×128 pixels on the detector. The final weight used for each equation was

$$w_t = w_\rho \cdot w_m \tag{14}$$

5.2 Implementation

We had two separate teams working on independent implementations of the algorithm. However, the SVD subroutine used by both codes are based on the SVD implementation given in the *Numerical Recipes* (NR). One of the codes was fully implemented in IDL, using the standard routines SVDC and SVSOL. The second implementation was in F77, using the routines as provided by NR. All computations in both codes are carried out in double precision. The two codes will be referred to as "R2C" and "MRC" and their implementations were extensively cross checked using mock catalogs (Sect. 6) before they were applied to the real data (Sect. 7).

5.3 Verification and test of the algorithm

Before application of the code to the VLT data we first applied it to a large number of simulated data sets. The two independent teams worked on simulated data production and were running the two independent codes as described in the above section. The two teams applied their codes to both their own simulated data, and to the ones from the other team for external verification. Simulated data were created in a hierarchy of increasing complexity using the following elements:

- **Stellar magnitudes.** Input magnitudes of stars.
- **Image zero-point off-sets.** The value of the global zero-point of each image (i.e. sky transparency).
- **Number of stars.** N: Number of stars within a single pointing.
- **Stellar grid.** Distribution of stars: Even grid, random distribution, observed grid.
- **Dither/rotation pattern.** We applied two basic patterns. Both patterns consisted of 4 rotations on a central field and in addition 4 off-set positions. The off-set frames (referred to as "dithers") were done either diagonally as seen from the CCD (8pssd4X) or along rows/columns (8pssd4+). The naming convention we use here is "8p" (8 pointings, in this work we always use 8 pointings, in FAP we used 28p), "ssd4X" (ss is the size of dithers given as fraction of the CCD size in %, d4 means 4 dither positions, X refers to the X-shaped pattern (diagonal). Our observed data set was taken with pattern 8p50d4X (half CCD size dithers diagonally). In the simulations we test both X and + patterns with dithers between 0 and 50%.
- **Random errors.** Measurement errors on individual magnitudes were set to values between 0 and 0.03 magnitudes. Random numbers picked from a normal distribution with the selected rms were added to the magnitudes of each "measurement" of each star.
- **Shape of input** *F(x,y)*. Order of polynomial and/or additional exponential.

The input *F(x,y)* was constructed in many ways, but was in all cases fitted by a polynomial form (Sect. 6). Because stars in general will not be evenly distributed across the field, the solution may become biased towards weighting areas with many stars more than areas with few stars. To compensate for this there is an option to apply "inverse surface density weighting" (for details see Sect. 5.1).

5.4 Graphical output format

For presentation of the results we decided on a graphical format where all the output of a given model run is shown on a single page. In Fig. 3 we show an example of such a run output page. In the top left of each page we give the definitions of each run in numerical form. The top line contains the "long identifier" which contains the run ID, the stellar grid, stellar magnitude model, random errors, zero-point model, and number of stars. The long identifier is also the name of the postscript output file. The "Run ID" is a running integer for easy reference in the run log. "Polyorder" is the definition of the input $F(x, y)$. In the simple cases this just gives the order of the input polynomial, but to test more complex shapes we also add exponentials. "Fit order" is the order of the polynomial we use for fitting. "Grid" defines the distribution of stars in the field, in the first runs this is set to "even" which is a uniform grid. "Pattern" refers to the offset pattern of the input frames. "Magnitudes" are the input definition of magnitudes of the grid stars ("equal" means that they are all the same). "Errors" gives the rms of the gaussian distribution of added random errors. "Zeropoints" is the input definition of the zero-points of each frame (step-size of difference). "N stars" is the number of stars in a single frame. Last three rows give the exact values of the input zero-points ("Zp in"), and the fitted zero-points of the two codes ("Zp R2C" and "Zp MRC").
The 3D plot at top right is the input $F(x, y)$ shape i.e. the shape the codes are trying to determine. The two central lines of plots are for the two different codes, upper for R2C and lower for MRC. They consist of a plot to the left where black circles depict the simple zero-point offset corrected input data and the magenta circles depict the photometry corrected with the $F(x, y)$ as determined by the code. The central 3D plots show the $F(x, y)$ correction shape that was found. On the right is a plot of the differences of the fitted and input zero-points. At the bottom are three 3D plots showing the differences between input and the two fits, and the difference between the two fits. The y-axis scale is the same in the upper 3 rows of 3D plots, but is scaled to the actual peak-to-peak residuals in the bottom three plots. The peak-to-peak scale is printed above each of the three bottom plots.

5.5 Basic verification

For input data without errors and with an input *F(x,y)* of a polynomial form, the fit should be perfect to within the computational accuracy. Fig. 3 shows the result from such a run (input 3rd order polynomial, fitted by 3rd order polynomial, no errors added), and it is seen that the fit is good to within a

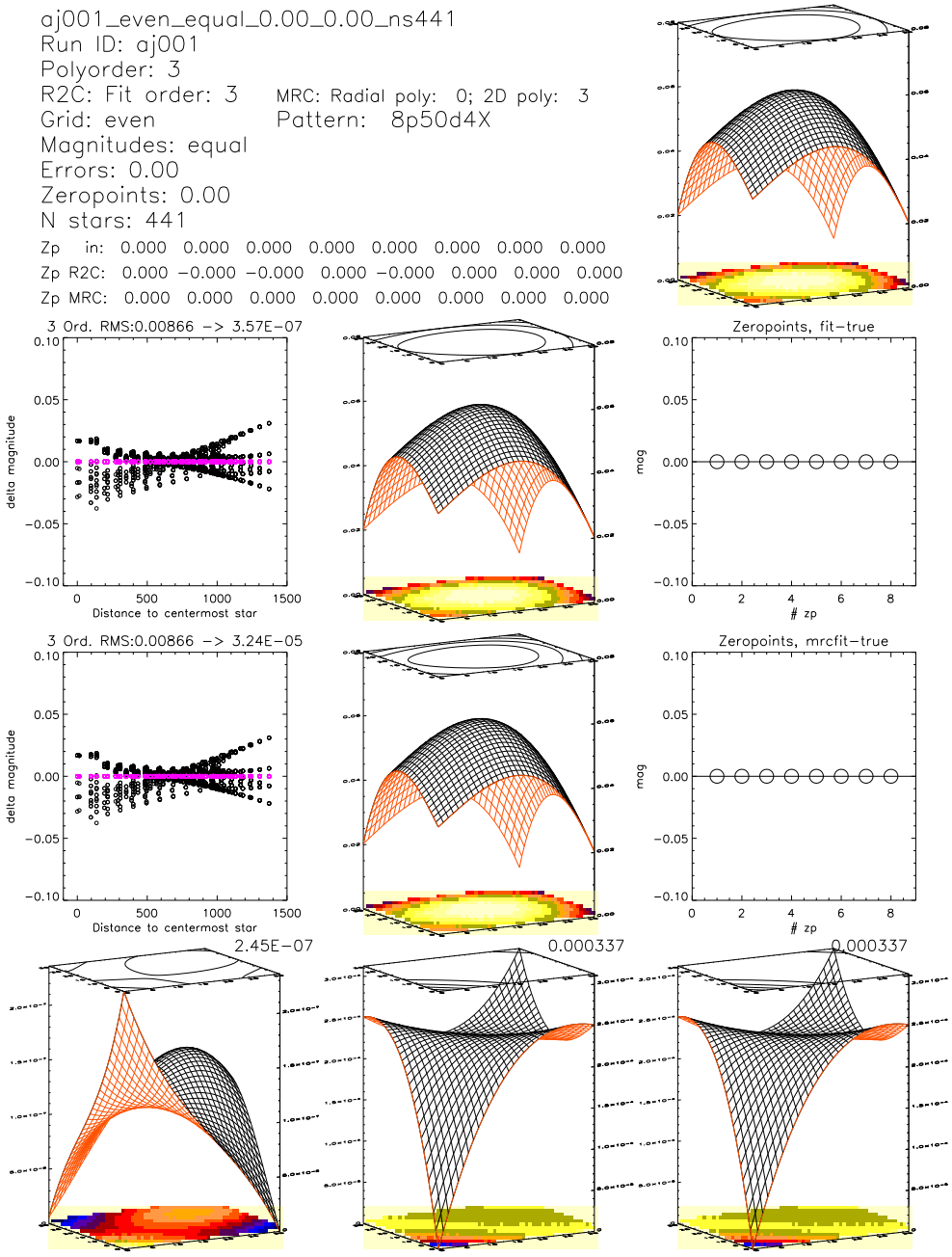
aj001_even_equal_0.00_0.00_ns441
Run ID: aj001
Polyorder: 3
R2C: Fit order: 3
MRC: Radial poly: 0; 2D poly: 3
Grid: even
Pattern: 8p50d4X
Magnitudes: equal
Errors: 0.00
Zeropoints: 0.00
N stars: 441
Zp in: 0.000 0.000 0.000 0.000 0.000 0.000 0.000 0.000
Zp R2C: 0.000 −0.000 −0.000 0.000 −0.000 0.000 0.000 0.000
Zp MRC: 0.000 0.000 0.000 0.000 0.000 0.000 0.000 0.000
3 Ord. RMS:0.00866 -> 3.57E-07
delta magnitude
Distance to centermost star
Zeropoints, fit−true
mag
zp
3 Ord. RMS:0.00866 -> 3.24E-05
delta magnitude
Distance to centermost star
Zeropoints, mrcfit−true
mag
zp
2.45E-07
0.000337
0.000337

Figure 3:

systematic error of 8.83e-8 (peak-to-peak over the entire field) in the R2C fit. For reasons we have not yet fully understood, the f77 implementation (MTC) does not do this quite as well (2.49e-4), but is still in a regime where it has no impact on our results. We take this to verify that computational errors of our code will not be a limiting factor.
As a by-product of the code we also determine the magnitudes of all stars in the field, and the zero-point offset of each individual frame. Again, as long as there are no errors, the magnitude of the input stars, and the zero-point offsets of the frames should not (to within computational error) have any influence on the results. To verify this the next two runs (e.g. Fig. 4) were identical to Run001, except that the stars had different magnitudes in Run002, and zero-points offsets were added in Run003. For both runs we found that the errors still are in the regime of computational errors.

6 Performance and accuracy of the algorithm

6.1 Metric / Figure of merit

Fig. 3-4 present examples of test runs. The errors on the determination of the correction frame ($F(x, y)$) are shown in the bottom plots. In order to quantify how well F is determined we decided to use the "peak-to-peak" (PTP hereafter) difference between input and output $F(x, y)$. PTP is the distance between the highest and the lowest value in the difference frame, i.e. it represents the variation of the photometric zero-point across the field. PTP is therefore the "worst case error". Alternatively one could choose the rms as metric, but since the error is systematic across the field we decided to use PTP. One should keep in mind that this is an over-estimate of the error in its usual meaning.

6.2 Photometric errors

Having verified the code we now explore its performance in parameter space. We start with an even (regular) grid of 441 stars and an input $F(x, y)$ which is a 2D, non-symmetric and off center, polynomial of 3rd order. We made 5 independent runs for each 5 different values of added photometric errors (two examples are shown in in Figs. 5 and 6). In Fig. 7 we plot the relation, and it is seen that it is well represented by a linear relation

$$PTP = 0.49 * rms$$

This empirical scaling relation is useful as it means that we can now limit ourselves to test only a single value rms value, and then later simply scale the results accordingly. The relation has a very small scatter for rms values less than 0.02, so we choose 0.01 for the following tests.

6.3 Number of stars

To test the influence of the number of stars, we used even grids of N stars, again an input polynomial of 3rd order, and photometric errors of 0.01 mags rms. We

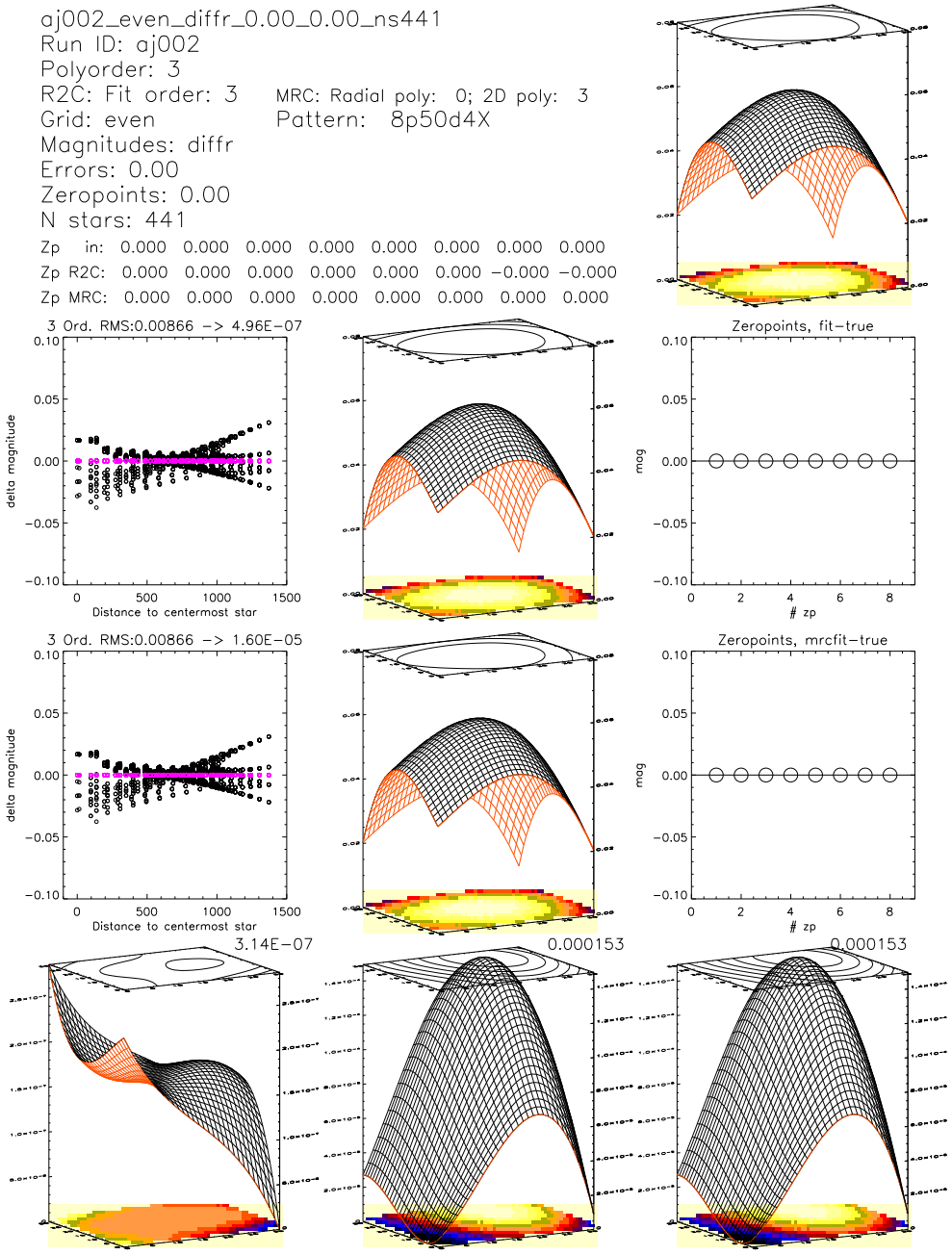
aj002_even_diffr_0.00_0.00_ns441
Run ID: aj002
Polyorder: 3
R2C: Fit order: 3
MRC: Radial poly: 0; 2D poly: 3
Grid: even
Pattern: 8p50d4X
Magnitudes: diffr
Errors: 0.00
Zeropoints: 0.00
N stars: 441
Zp in: 0.000 0.000 0.000 0.000 0.000 0.000 0.000 0.000
Zp R2C: 0.000 0.000 0.000 0.000 0.000 0.000 −0.000 −0.000
Zp MRC: 0.000 0.000 0.000 0.000 0.000 0.000 0.000 0.000
3 Ord. RMS:0.00866 -> 4.96E−07
delta magnitude
Distance to centermost star
Zeropoints, fit−true
mag
zp
3 Ord. RMS:0.00866 -> 1.60E−05
delta magnitude
Distance to centermost star
Zeropoints, mrcfit−true
mag
zp
3.14E−07
0.000153
0.000153

Figure 4:

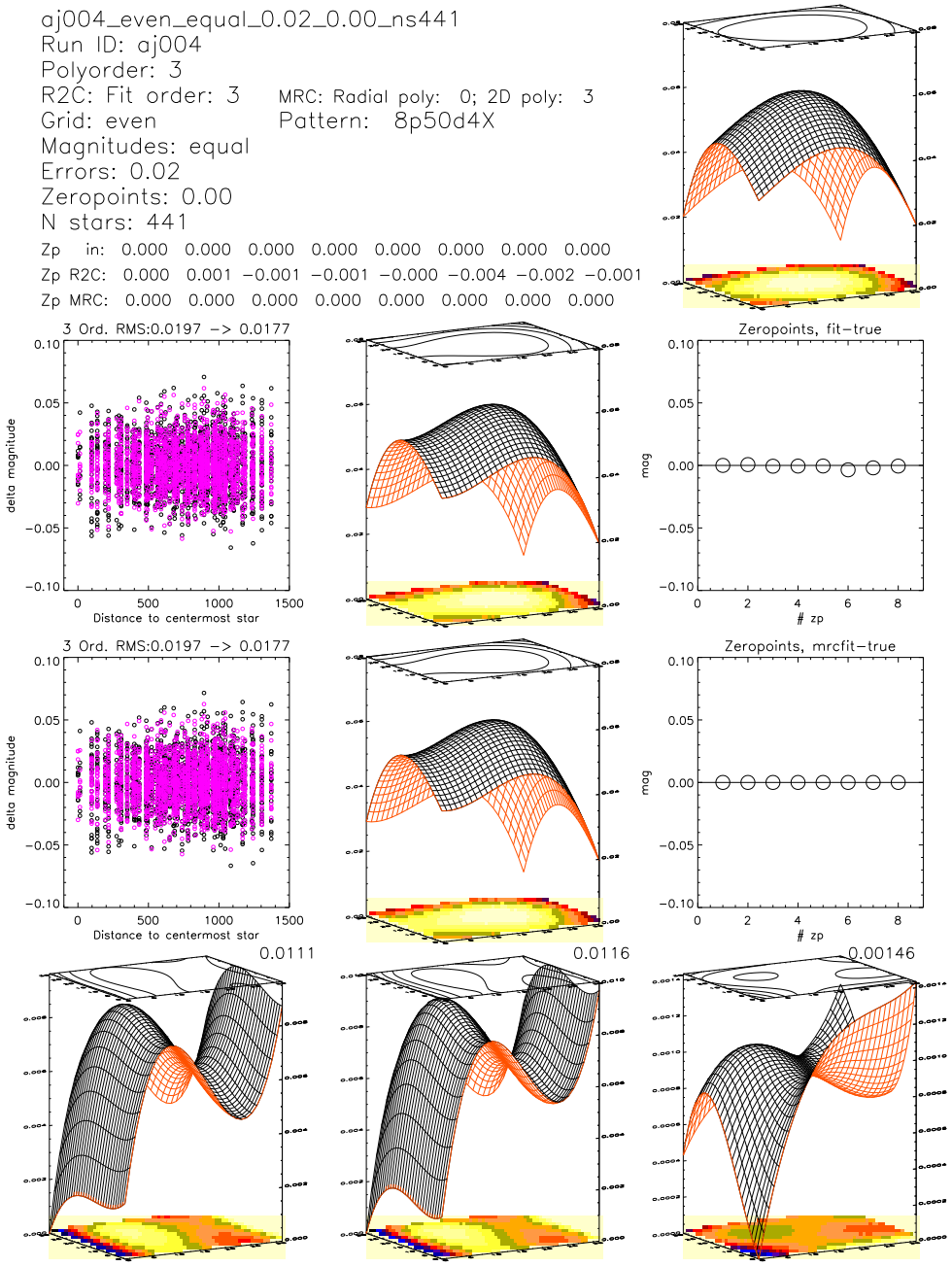
aj004_even_equal_0.02_0.00_ns441
Run ID: aj004
Polyorder: 3
R2C: Fit order: 3
MRC: Radial poly: 0; 2D poly: 3
Grid: even
Pattern: 8p50d4X
Magnitudes: equal
Errors: 0.02
Zeropoints: 0.00
N stars: 441
Zp in: 0.000 0.000 0.000 0.000 0.000 0.000 0.000 0.000
Zp R2C: 0.000 0.001 −0.001 −0.001 −0.000 −0.004 −0.002 −0.001
Zp MRC: 0.000 0.000 0.000 0.000 0.000 0.000 0.000 0.000
3 Ord. RMS:0.0197 -> 0.0177
delta magnitude
Distance to centermost star
Zeropoints, fit−true
mag
zp
3 Ord. RMS:0.0197 -> 0.0177
delta magnitude
Distance to centermost star
Zeropoints, mrcfit−true
mag
zp
0.0111
0.0116
0.00146

Figure 5:

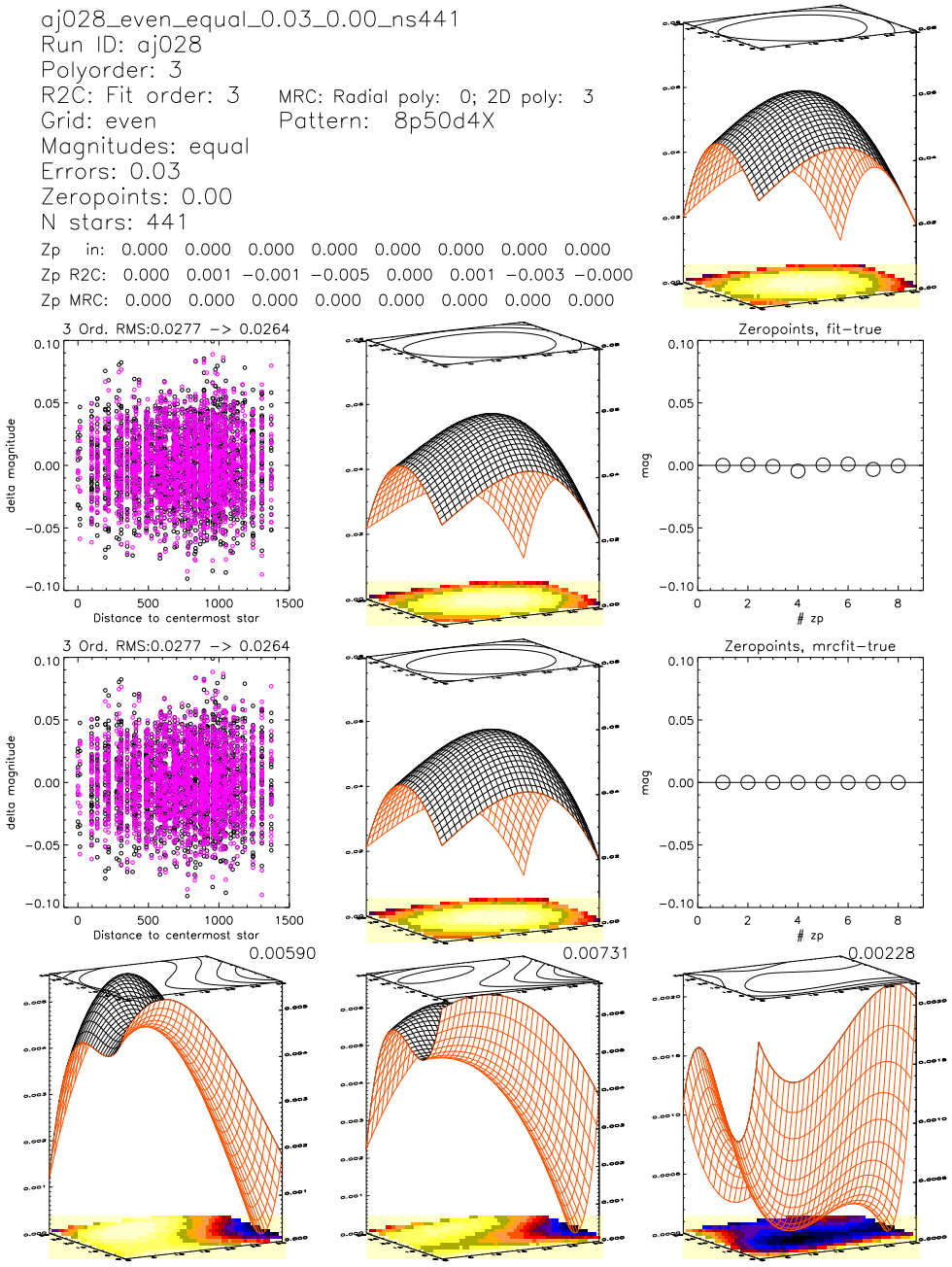
aj028_even_equal_0.03_0.00_ns441
Run ID: aj028
Polyorder: 3
R2C: Fit order: 3
MRC: Radial poly: 0; 2D poly: 3
Grid: even
Pattern: 8p50d4X
Magnitudes: equal
Errors: 0.03
Zeropoints: 0.00
N stars: 441
Zp in: 0.000 0.000 0.000 0.000 0.000 0.000 0.000 0.000
Zp R2C: 0.000 0.001 −0.001 −0.005 0.000 0.001 −0.003 −0.000
Zp MRC: 0.000 0.000 0.000 0.000 0.000 0.000 0.000 0.000
3 Ord. RMS:0.0277 −> 0.0264
delta magnitude
Distance to centermost star
Zeropoints, fit−true
mag
zp
3 Ord. RMS:0.0277 −> 0.0264
delta magnitude
Distance to centermost star
Zeropoints, mrcfit−true
mag
zp
0.00590
0.00731
0.00228

Figure 6:

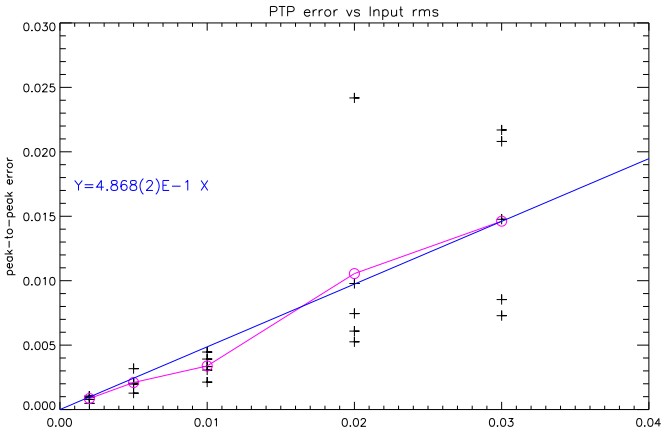

Figure 7: Systematic peak-to-peak (PTP) error across the field as a function of the input rms random error (for 441 stars per frame). "+" marks individual runs (five for each rms value), circles mark the mean of the five.

made 5 independent runs for each of several values of N. Two representative output pages can be found in Figs. 8 and 9 and the relation we found is shown in Fig. 10.
From Fig. 10 we see that (as one would expect) the fit gets better as we add more stars in the field. However, the PTP almost levels out around 250 stars, and only improves very slowly at higher values. A fit to the points above $N = 250$ gives this empirical relation:

$$PTP = 0.0059 - 2.15 \times 10^{-6} N$$

The slower drop at high N is caused by several stars sharing the same (redundant) information. Based on the tests in Sections 6.2 and 6.3 we conclude as follows: For a given value of N, PTP grows rapidly with the photometric error. For a given input photometric error PTP improves rapidly with N until $N = 250$ but only slowly after that. Therefore, it is advisable to have a field with ≈ 250 stars, but if increasing the number of stars beyond that requires to lower the signal-to-noise cut significantly, then it is better to keep the higher S/N cut and fewer stars. The "transition value" of N (in this case 250) is possibly a function of the off-set pattern used, and also of the actual distribution (clumping) of stars in the field. We shall address those points below.

6.4 Fitting order

So far we have been creating input $F(x, y)$ as a 3rd order polynomial, and subsequently tried to fit it with a 3rd order polynomial. This was useful for verification purposes, but in the general case we cannot use this simplifying assumption. For all subsequent tests we shall therefore use functions that cannot be perfectly fit by a low order polynomial. Here we use a 3rd order polynomial with an added exponential. In order to determine how best to fit such a general functional form, we again simulate data with several different values of N (121, 225, 361), but with no photometric errors (Run092 through Run115). We then

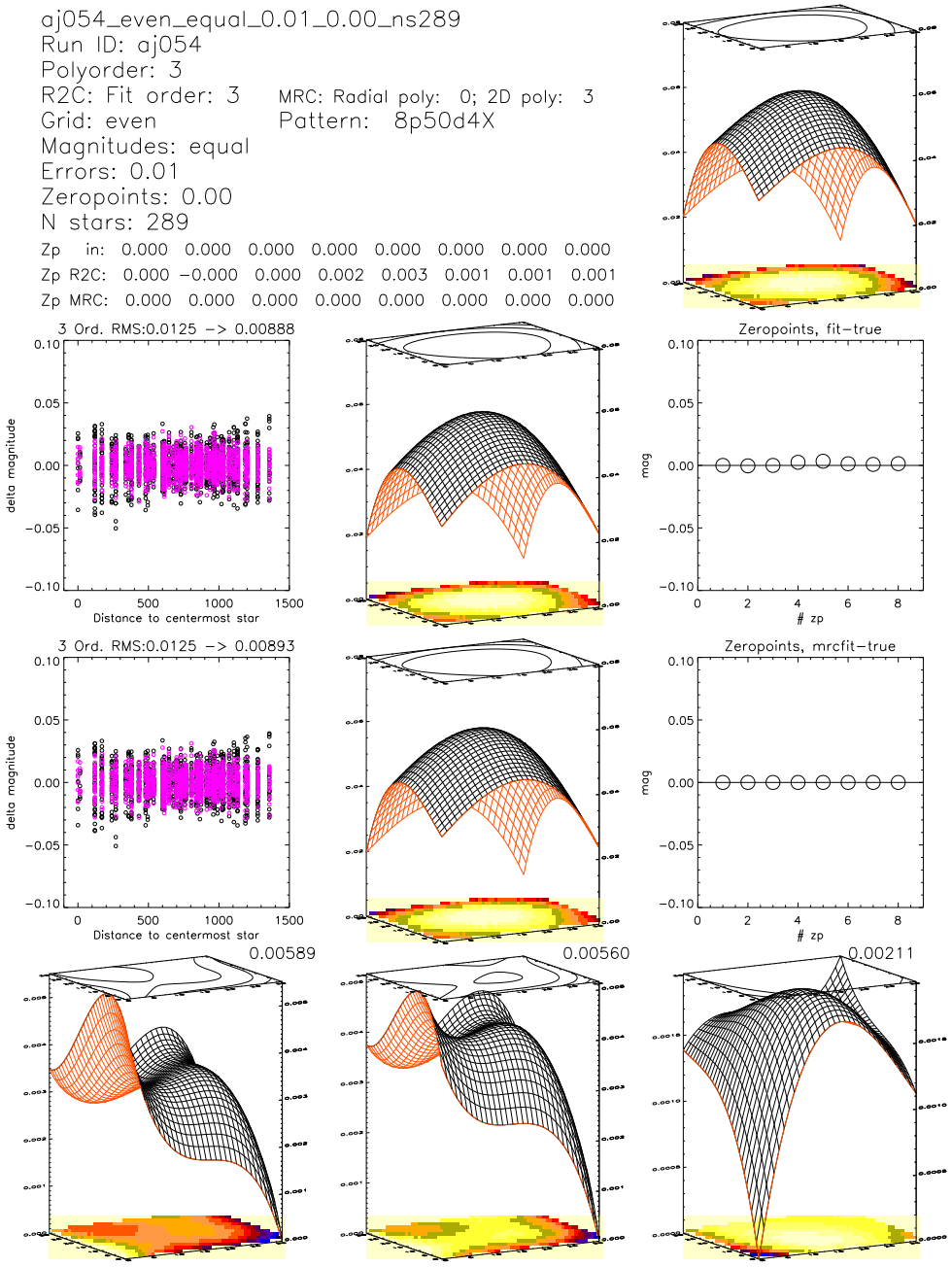
aj054_even_equal_0.01_0.00_ns289
Run ID: aj054
Polyorder: 3
R2C: Fit order: 3
MRC: Radial poly: 0; 2D poly: 3
Grid: even
Pattern: 8p50d4X
Magnitudes: equal
Errors: 0.01
Zeropoints: 0.00
N stars: 289
Zp in: 0.000 0.000 0.000 0.000 0.000 0.000 0.000 0.000
Zp R2C: 0.000 −0.000 0.000 0.002 0.003 0.001 0.001 0.001
Zp MRC: 0.000 0.000 0.000 0.000 0.000 0.000 0.000 0.000
3 Ord. RMS:0.0125 −> 0.00888
delta magnitude
Distance to centermost star
Zeropoints, fit−true
mag
zp
3 Ord. RMS:0.0125 −> 0.00893
delta magnitude
Distance to centermost star
Zeropoints, mrcfit−true
mag
zp
0.00589
0.00560
0.00211

Figure 8:

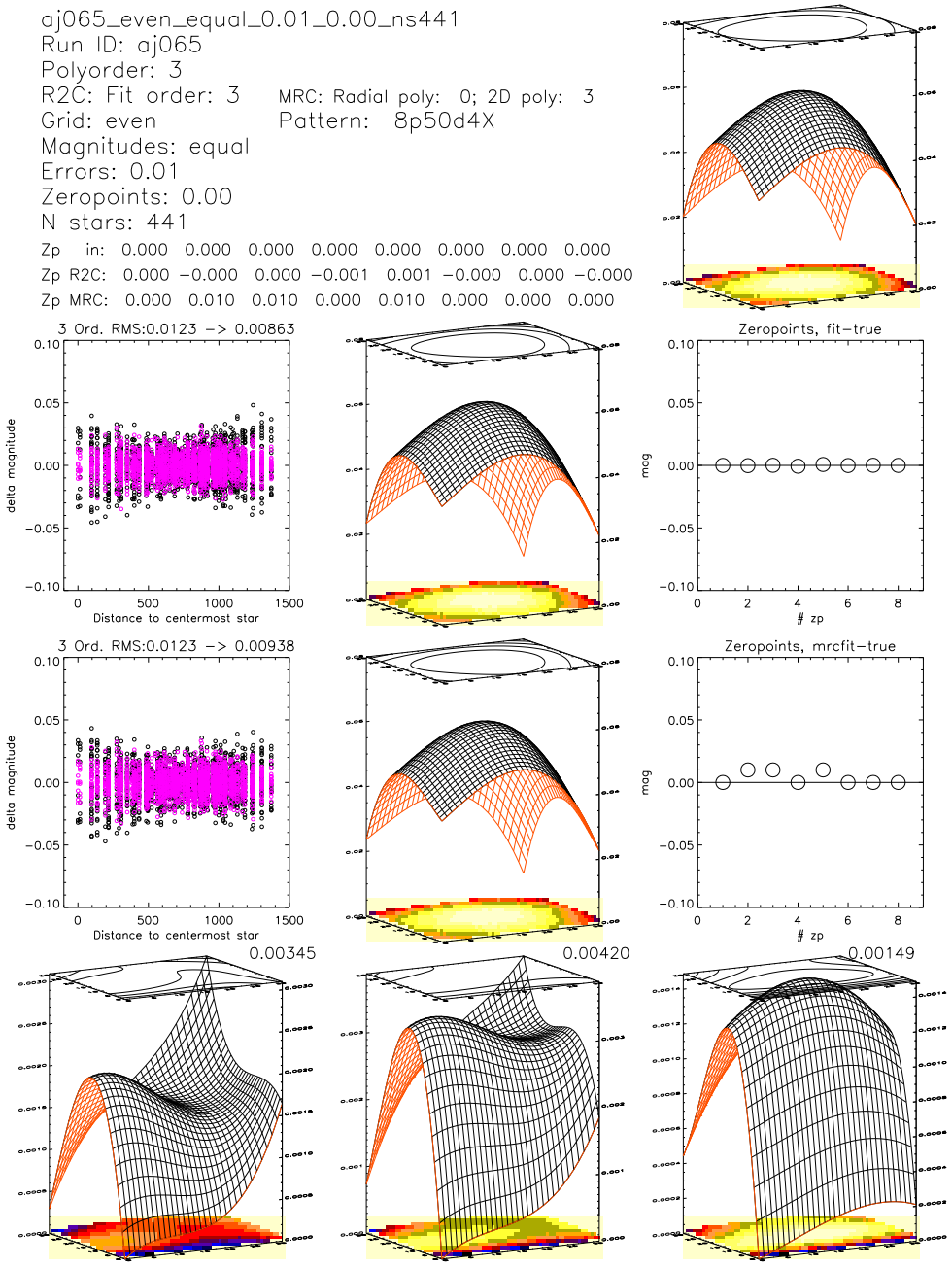
aj065_even_equal_0.01_0.00_ns441
Run ID: aj065
Polyorder: 3
R2C: Fit order: 3
MRC: Radial poly: 0; 2D poly: 3
Grid: even
Pattern: 8p50d4X
Magnitudes: equal
Errors: 0.01
Zeropoints: 0.00
N stars: 441
Zp in: 0.000 0.000 0.000 0.000 0.000 0.000 0.000 0.000
Zp R2C: 0.000 −0.000 0.000 −0.001 0.001 −0.000 0.000 −0.000
Zp MRC: 0.000 0.010 0.010 0.000 0.010 0.000 0.000 0.000
3 Ord. RMS:0.0123 -> 0.00863
delta magnitude
Distance to centermost star
Zeropoints, fit−true
mag
zp
3 Ord. RMS:0.0123 -> 0.00938
delta magnitude
Distance to centermost star
Zeropoints, mrcfit−true
mag
zp
0.00345
0.00420
0.00149

Figure 9:

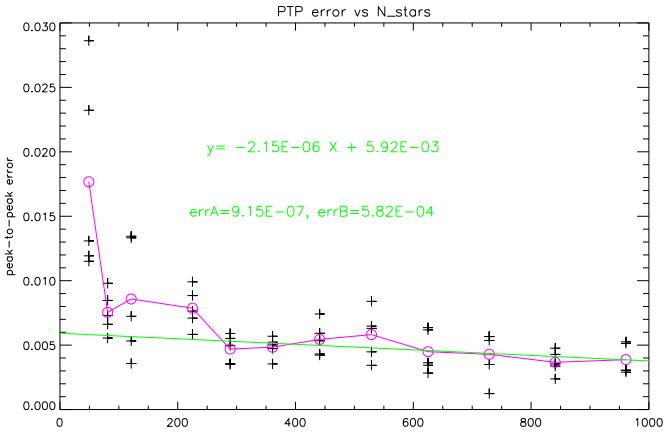

Figure 10: PTP error across the field as a function of the number of stars in each image. "+" marks individual runs (three for each rms value), circles mark the mean of the three.

obtain the best fits with polynomials of several different orders. The results (see Fig. 11) show that for 121 stars (11×11 grid) the best fit is obtained with a polynomial of order 3, while for 15×15 and 19×19 a 4th order fit is slightly better. The fit is no longer as perfect as in the simple case (e.g. Fig. 3), but it is still excellent ($PTP \approx 4^{-4}$).

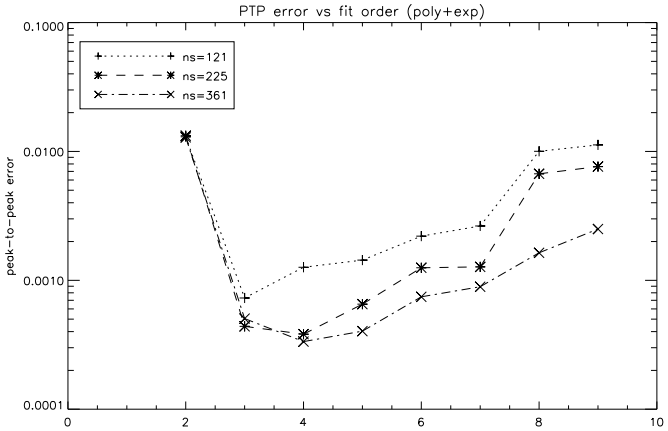

Figure 11: PTP error as a function of the fitting order. Different symbols correspond to different value of N-star. Depending on the value of N-star the best fit is found with either a 3rd or a 4th order polynomial.

We now return to the relation between the quality of the fit as a function of input rms (Fig. 11) to see if how this will change for a more complex functional shape. We therefore repeat the same runs as for Fig. 11, but now using the generalised input function and fitting with a 3rd order polynomial (Run141 through Run200). The results (Fig. 12) show that in the general case the PTP(rms) is the same as for the simple case, even the scaling relation remains unchanged.

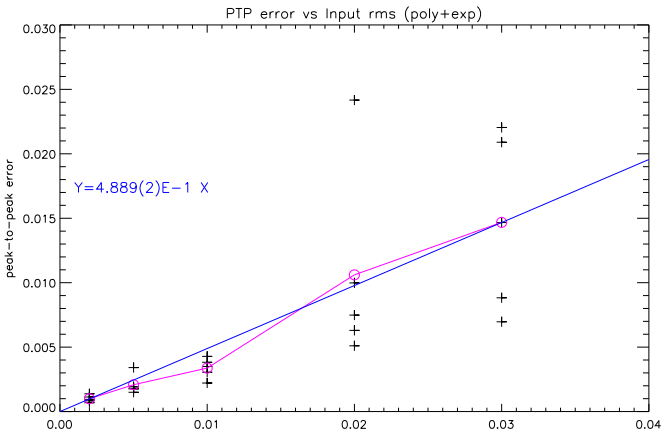

Figure 12: PTP error across the field as a function of the input rms random error (for 441 stars per frame) and an exponential component in the input F. "+" marks individual runs (five for each rms value), circles mark the mean of the five.

6.5 Offset size and pattern

The exact offset pattern, the number of dithers, number of rotations, and dither step sizes, those parameters will all influence the accuracy of the fit. It has already been demonstrated (Sect. 4.2) that both rotations and dithers are needed in order to constrain the solution. For dithers there are two issues to consider. *(i)* Small dithers provide very poor information about the gradient of F across the field, large dithers provide much better information in this respect. *(ii)* Small dithers cause only a very small loss of objects as they fall off the edges of the common field, lager dithers will drop more objects off the edge.

Taken together this means that for very small offsets we expect poor fits, increasing the offset size should cause the PTP error to drop, but at large enough offset sizes we start running out of objects, and we expect the error to grow again. The exact position of the minimum is likely to depend on many factors. In Fig. 13 we explore some of those. In all cases we used 4 rotations 90 degrees apart and an even grid of 441 stars. We tested both diagonal offset patterns ("X", runs 306-350), and row/column offset patterns ("+", runs 261-305). The offset sizes are in percentage of the entire CCD field. It is seen that the expectations pretty much are confirmed. Offset sizes less than $\approx$10% of the field are found to be too small, while offsets of 20-30% appear to be optimal for the number of stars used. For the "+" pattern it stays good even for 50% offsets, for the "X" we run out of stars twice as fast as for "+" and the PTP error starts to rise, albeit slowly.

For the rotations a similar line of arguments can be applied. 90 degree rotations would seem optimal because there is 100% overlap of the rotated fields. From Fig. 13 we also see that if the input F is rotational symmetric then the fits are extremely poor for small offsets. This is because the 4 rotated frames contribute no information when F is rotational symmetric. It would seem that the optimal offset size for "X" patterns is 20 - 30% of the CCD size, and for "+" patterns 20

- 50%.

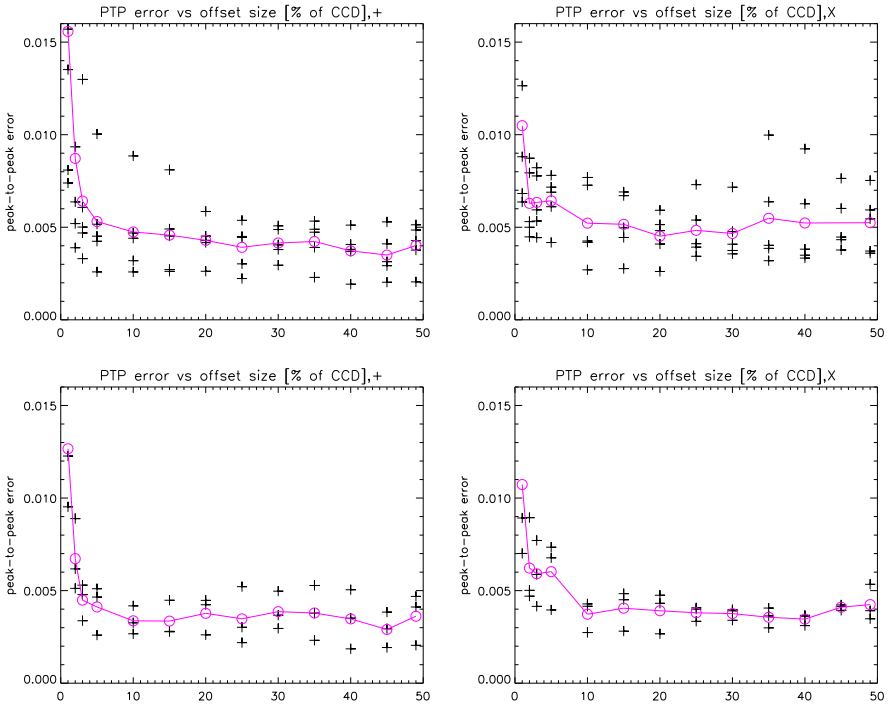

Figure 13: *PTP* error as a function of the dither offset size (in percent of the CCD field size). **Top left:** "+ offset" pattern, F rotationally symmetric. **Top right:** "X offset" pattern, F rotationally symmetric. **Bottom left:** "+ offset" pattern, F asymmetric. **Bottom right:** "X offset" pattern, F asymmetric.

7 Application to FORS1 test data

7.1 Test run B and R data

In 2004 we obtained a first set of test data. The data were all obtained on the same non-photometric night and consist of 13 frames in B and 20 frames in the R band. In B, we have 4 images without offsets with different rotation angles (180,90,0,-90), and 4 offset positions, in total 13 images of the field. All exposure times in B are 5 seconds. In R, we have 4 images without offsets with the same rotation angles as in B and 4 offset positions with 2 to 3 images per position. For all pointings/rotations there are 2 and 1 second exposures. The offset pattern we used (8p50d4X) is shown in Fig. 2, and the basic reductions were described in detail in Report I.

Photometric measurements were done using the DAOphot photometry package in Iraf and IDL in two phases; first aperture photometry and then PSF fitting of the well behaved stars (normal DAOphot procedure). The results were confirmed to be identical irrespective of the software environment used. The photometry on the individual frames was registered onto the central frame. Then the (X, Y) coordinates and magnitudes and errors were collected into a

single table, with one star per line, one group of columns per frame.
The photometric data were filtered through a cleaning procedure as follows. First all measurements with reported DAOphot errors larger than a set limit (typically this would be set to 0.01, 0.02 or 0.03 magnitude) were rejected. Then, for each star, the median and the std. dev. of all measurements were computed and an iterative sigma clipping loop was applied. This latter step was to remove bad measurements (e.g. stellar psfs hit by cosmics).

7.2 Results of test run

We applied the method developed and tested in the previous sections to the photometric output from DAOphot. Here we report the results.

7.2.1 *R* band data

In the R band we have 77 stars with DAOphot 1σ errors less than 0.01 mag, 72 with 1σ in the range 0.01 to 0.02, and 43 stars in the range 0.02 to 0.03 mag. The fitting code uses an inverse variance weighting scheme (Equ. (12)), so inclusion of the fainter stars does not add in linear relation to the number of stars. We fitted with 77 ($\sigma \leq 0.01$) stars, with 149 ($\sigma \leq 0.02$), and with 192 ($\sigma \leq 0.03$) stars. The resulting correction frames f are shown in Fig 14 where we also show the distribution of the measurements on the CCD. As seen from Fig. 14 we have a very even distribution of measurements across the field, but still the process of fitting a low order polynomial could possibly be producing spuriously large gradients at the edges of the frame. We shall return to this question below.

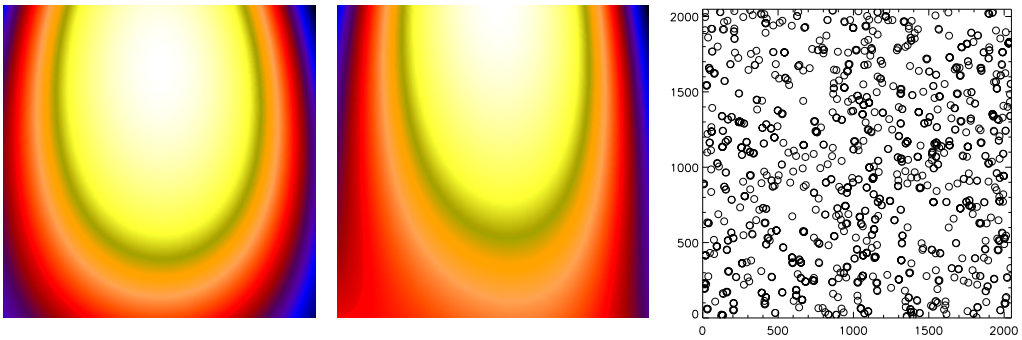

Figure 14: R band correction frame f (see Equ. (3)) calculated using stars clipping at $\sigma = 0.01$ mag (left) and at $\sigma = 0.03$ mag (middle). Right: The actual distribution, on the CCD, of all observations of only the 77 best stars (clipping at $\sigma = 0.01$ mag). Note that measurements cover the field evenly.

The correction frame F (or f in delta magnitude form) is a combination of the TSI and the QEF (Equ. (1)). If the QEF is very flat and smooth (i.e. close to $QEF(x, y) = 1.00$ over the entire frame) then F is almost identical to TSI. If, on the other hand, the QEF is strongly variable across the field, then those variations will dominate the TSI which will in that case not at all resemble F. It is therefore interesting to ask how strong a correlation we find

between f and TSI. If there is a very strong correlation then it means that the CCD intrinsically has a very flat response and that there is no strong vignetting of the field. In that case a calibration procedure simply involving "flattening" the TSI by division of a smoothed version of itself would produce a very good calibration without need for further correction. If, on the other hand, we see no such correlation then it means that there are dominating features in the QEF, and then the simple "flattening procedure" would introduce errors rather than correct them.

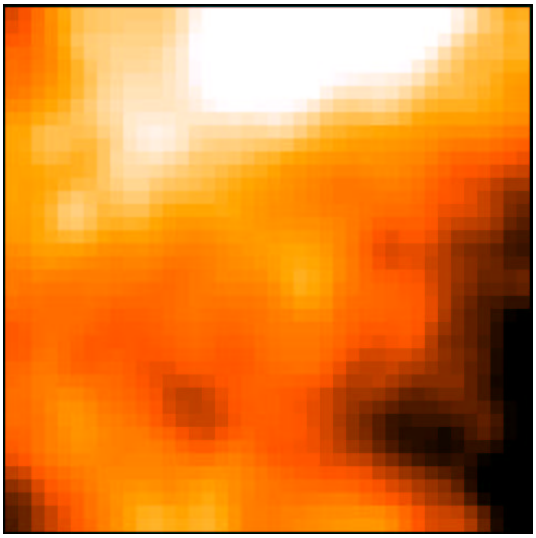

Figure 15: The R band twilight sky image (TSI), heavily binned. Peak-to-peak variation across the field is 4%. Notice the global similarity to the f frames shown in Figs. 14 and 16.

With this in mind we reproduce, in Fig. 15, a smoothed and heavily rebinned plot of the twilight image we used. We see immediately that there is some large scale resemblance to f. They both have their brightest peak at the top center, low values at the corners, and a general slope from top to bottom. The slope is presumably an actual slope on the twilight sky, which was found and corrected by the algorithm. However, we also see that there is not a one-to-one correspondence between the two frames and that there are many features on small scales that are present only in the TSI. Those small scale features could be either real features of the QEF, or they could be small scale features of the TSI only. If the latter is the case, then our algorithm failed to find them because their scale is too small to be fitted by a 3rd order polynomial.
To investigate if there is evidence for structure on smaller scales we increased the order of the polynomials to 4, 5 and 6, and the results are shown in Fig. 16. Only very small changes are seen when increasing to 4th and 5th order. This means that no important features are present on those scales, and supports our general assumption of large scale features only. The 6th order fit suddenly breaks up into many small fragments, but our data were not taken with the purpose to look for features on those scales (which would require more dither points) so it is not clear if those features are real small scale features or simply

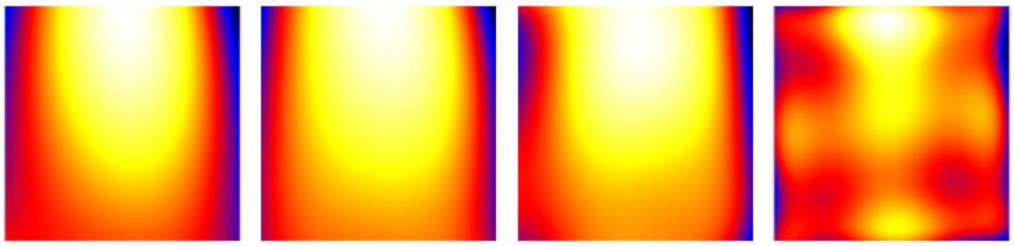

Figure 16: R band correction frame f, fitted with polynomials of order 3, 4, 5 and 6 (left to right).

a result of too few data-points fitted with a too high order polynomial. A new data set with many more dithers is already being analysed as part of the FORS Absolute Photometry project (FAP). The FAP project will be addressing the issue of small scale features. With the higher order fits we can now re-address the question from earlier whether the low order fit produced spurious steep gradients at the edge of the field thereby increasing the PTP. If that was the case then a higher order fit provides the possibility to modify the steep gradients at the edges and decrease the PTP. In fact what we see is an increase in PTP.

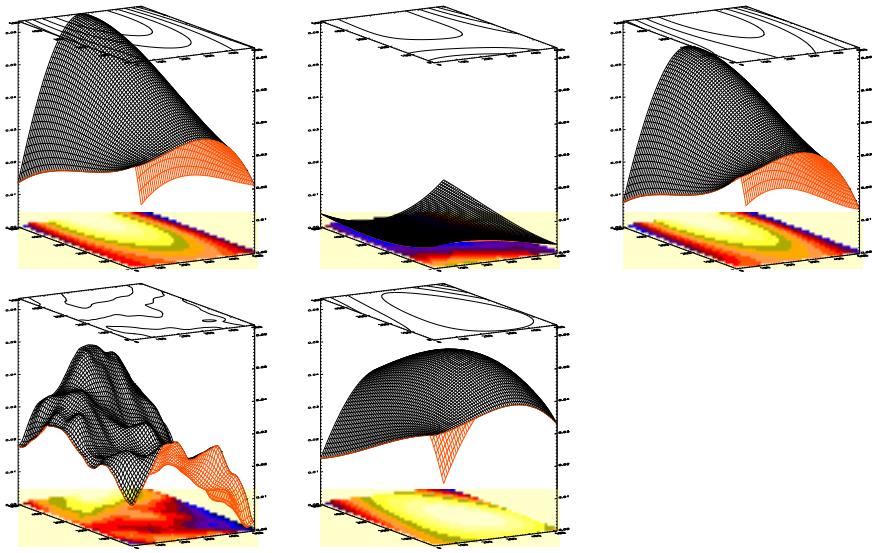

Figure 17: **Top left:** 3D representation of the R band f frame. **Top middle:** Iteration on the fit, i.e. applying the correction found (left), fitting to the residuals after sigma clipping rejection. **Top right:** Sum of fit and iteration, this is the actual correction frame f. **Bottom left:** 3D representation of Fig. 15, the smoothed R band TSI. **Bottom right:** Correction frame f after experimentally removing the signature of the smoothed TSI.

The resulting correction frames in Fig. 14 were the results of fits to the data set after a sigma clipping. Since the sigma clipping was performed on data that had been modulated by the signature of f, part of the signal we are looking for may

have been removed, or enhanced, by the clipping. We therefore subsequently applied an iterative procedure where we corrected the input photometry with the f field found, then applied the clipping to those corrected data, and performed a fit to the corrected data. The procedure is illustrated in Fig. 17 where we show the 3D representation of the first fit to the f frame (upper left), then the fit to the corrected data set (upper middle plot). It is seen that the residuals are small, but not negligible. The corrected f frame is shown in the upper right figure. All three on the same scale. The peak-to-peak (PTP) of the left figure is 0.063 magnitudes, but after the first iteration (upper right) this has fallen to 0.054 mag. Additional iterations do not change this. Even if we ignore the edges and the corners of the largest variations, we find that over 90% of the frame the variations are still 0.034 mag PTP.
As pointed out above there are some large scale similarities between the f frame we determine, and the TSI. Those similarities are displayed in 3D in Fig. 17 upper right (final f frame) and lower left (smoothed TSI). As mentioned above, one may therefore imagine that a simple "flattening procedure" of the TSI would improve the calibration. We tested this assumption by applying a correction to our photometric data by effectively use the lower left figure as an f frame, and then to make a fit to the residuals. The resulting fit is shown in the lower right figure. As expected it is seen that it is indeed in general flatter than the f frame above it. The PTP is still fairly high though (0.051 mag), but it can be seen that a large part of that is caused by a dip in one single corner. As already pointed out in Sect. 2, there seems to be an issue in the corners of either variable vignetting or a variable scattered component.

7.2.2 B band data

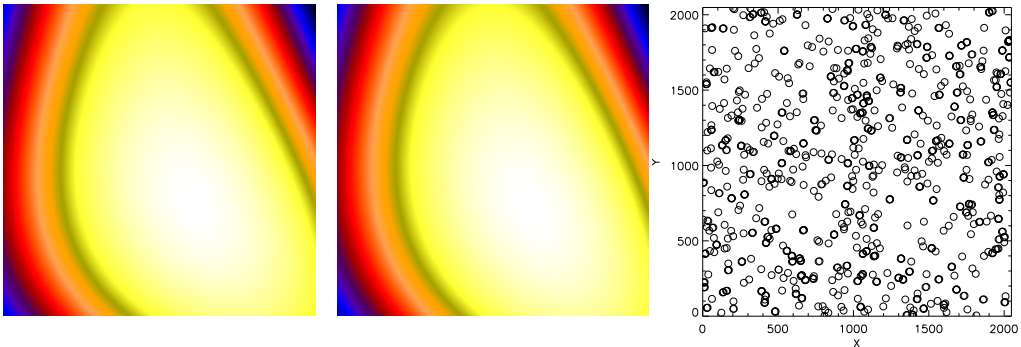

Figure 18: B band correction frame f (see Equ. (3)) calculated using stars clipping at $\sigma = 0.02$ mag (left) and at $\sigma = 0.03$ mag (middle). The variation of f across the field is 0.066 mag PTP. Right: The actual distribution, on the CCD, of all observations used in the fits.

For the B band data we followed the same procedure as outlined above, and arrived at similar conclusions. The B band f frame is shown in Fig.18.

7.3 Significance tests of the illumination correction

We can get a rough estimate of the significance of the results from the plots of Sect. 6. The scaling with input errors tells us that if we consider only 0.01 mag errors, then for an even grid of 441 stars the typical error on PTP is 0.005 mag. From Fig. 10, however, we see that since we have only 77 stars below 0.01 mag error, the error on PTP should be scaled up by a factor 2.5. The fact that our stars are not on an even grid works to increase this a bit more, but adding the extra stars with larger errors works the opposite way, neither effect is large, so they will roughly cancel to the first order. We conclude that the rough error is of the order 0.013, so the result is that for our R band F we measure $PTP = 0.054 \pm 0.013$ mag, i.e. a 4σ detection.
To test that our scaling relations indeed work we also carried out an exact simulation test. As input we gave an F with a PTP of 0.06 mag, as stellar grid we used the grid defined by our 77 best stars, and the input rms was 0.01 mag. We ran 10 different simulations and found that the error on recovery of F in this case was 0.013 ± 0.003.

7.4 Summary of results

In way of summarising what we have found we conclude the following:

- Even with a fairly mediocre dataset (short exposures, non-photometric conditions, small number of high S/N stars in field, and in retrospect not using the optimal offset pattern) our final PTP error is only 0.013 ± 0.003 mag.
- We determine, at 4σ, the correction frames applicable for the TSI's we used. They have $PTP = 0.054 \pm 0.013$ (R band) and 0.066 (B band).
- We have verified that for future purposes, our scaling relations reported in Sect. 6 can be used to determine errors.

8 Concluding remarks

8.1 Discussion of results

Data presented in Patat (2003) and in two recent FORS-IOT reports (Järvinen *et al.*, 2005; Mignani and Petr–Gotzens, 2005). suggest that with the currently used twilight image calibration method, significant variations of the photometric zero-point across the FORS fields are expected. In this report we measure the amplitude of those variations on FORS1, and we find that they are, for the night of our observations, 0.054 magnitudes across the field (peak-to-peak). The peaks of the distribution are found in the corners while over most of the field we have variations less than 0.034 magnitude. This can be thought of as a systematic error of ± 0.02 magnitude across the field, which is well within the 10% calibration accuracy ESO guarantees, assuming that the absolute zero-point calibration is better than a few %. A zero-point variation across the field of 0.054 magnitude does, however, make certain types of science requiring high precision photometry impossible, and we have here described in detail how this effect

best can be determined and corrected for. With a large number of simulated data sets we have produced scaling relations that can be used to determine the optimal observing strategy for a given target photometric accuracy.
The cause of the zero-point variation is a sum of at least two components: An instrumental effect known as "central light concentration" (presumably constant in time but this would have to be tested) and a twilight sky gradient (variable from night to night). We see evidence for other (short term time variable) effects also. The cause of those is not clear at present, but they should be addressed in the FAP project. The time variability means that each twilight image requires a separate correction term to be measured and calculated.
Tests (see discussion in Sect. 2) did not reveal any evidence for changes in the pixel-to-pixel variation of the quantum efficiency of pixels over a 6 month period. It therefore seems that an efficient calibration strategy may be to determine accurate master calibrations following the procedure outlined in this report. Such master calibrations should be checked nightly for changes (e.g. dust specks) but would then only need to be re-created when actual changes are seen.

8.2 Conclusion regarding obtainable accuracy

We have demonstrated that the method we have developed can produce photometric zero-point corrections to, in principle, any target precision. The limiting factors on the nominal accuracy to consider are:

- Signal-to-noise of twilight sky image (TSI).
- Number of stars in stellar grid.
- Photon noise of individual stellar images.

The S/N of TSI can be pushed up to almost any value simply by adding enough exposures. By careful selection of a set of optimal stellar fields, it should be possible to define grids with several hundred good stars at a handful of different RAs. The S/N (from photon noise alone) of individual stellar images is easily above 100 in a single exposure, and could be as high as 1000, but only for a very few objects in a given exposure as those will be just below saturation. The only way to go significantly above this would be to stack several images, but then one may as well use additional dither positions and get this extra information effectively for free. The S/N increases as the root of the number of exposures. The above is valid only if the following two assumptions are true:

- No time variability of QEF.
- There are no features of F on scales smaller than they can be determined by our chosen functional form.

For a correction field $F(x, y)$ that does not have significant power on small scales, we have seen that even a comparatively simple data set, such as the one used in this report, produces data with a constant zero-point across the entire field to within 13 millimag PTP. Carefully selecting a field of ≈ 300 stars (instead of the 77 available in this data set) immediately reduces this by a factor 2.5 (Fig. 10), and if one then doubles all exposures this would provide another factor 1.4 (Fig. 12) for a total PTP error of $13/(2.5 \times 1.4) = 3.7$ millimag.

In conclusion, following the strategy outlined in this report we see no particular problems preventing us from limiting large scale zero-point variations across the CCD to 4 millimag PTP for reasonable investments of observing time. It may well be possible to lower it further, but in that case the required observing time will increase significantly as we would need many more dither positions. For a very large number of dither positions, colour terms due to variable airmass may become an issue that one would need to consider.

8.3 Secondary Standards for the VLT, a realistic project?

We shall return now to the long standing question of how one may produce a useful set of secondary standards for current and future large aperture telescopes. Any such set of standards will not actually be truly "secondary", but will define the next step of a long climb down from Vega. As starting point we will need to use the Landolt fields (and fields derived from those). The stated goal of a secondary standard project, if such a project is started, should be to obtain magnitudes with standard errors $\sigma \leq 0.003$ magnitude for a large number of objects within each FORS field, covering a wide range in colours. The optimal aim would therefore be 1 milli-mag intrinsic error, but one could even accept 2 milli-mag.
In the previous section we found that 4 milli-mag PTP is a realistic goal with our method. How does this PTP relate to standard errors? The PTP is a systematic variation across the field and represents the extreme values. Within about 70-80% of the field the variation is typically on half of the PTP, so PTP can reasonably be regarded as the full $\pm 2\sigma$ range. In this interpretation the goal of 0.001 magnitude 1σ errors is achieved, but it is important to keep in mind that there is strong systematic error-correlation across the field. I.e. errors do not necessarily go down by $N^{0.5}$ when N measurements or objects are combined. The shutter time test (Patat and Romaniello, 2005) indicate that to guarantee an accuracy of 0.001 mag requires 10 second or longer exposures. This requirement, together with the need to link the observations to Landolt stars, makes such a project unfeasible with the VLT. A smaller (by about a factor 10) aperture is needed. A 2m class telescope with a similar instrument and similar field size would be ideal for the purpose. A wide field type instrument (such as e.g. WFI) would a first glance seem optimal because of the large number of Landolt stars that could be observed simultaneously. However, the large field also means that the F correction frame likely will have much larger PTP and consequently will be much harder to determine to the needed accuracy. The Danish 1.5m on La Silla has a bit smaller aperture (3.5% of a VLT UT), but the field size is good and the DFOSC instrument is of a type similar to the FORS. Illumination pattern corrections have already successfully been calculated for this instrument (Andersen, Freyhammer and Storm, 1995).

8.4 Secondary Standards, are they still needed?

The need for standards for large aperture telescopes has been recognized not only at ESO, but also in the community at large, and at least two groups have been

active in the field (Stetson, 2000; Saha, Dolphin and Thim, 2005). The Stetson fields are already in use for the calibration of VIMOS. Before embarking on a larger project to define secondary standard fields one needs to carefully look at the new sets available and ask the following questions: Are they accurate enough? Do they supply magnitudes for all the bands we need to calibrate? Are there enough high quality standards within a FORS field? Do they cover a wide enough spread in colours to determine colour terms?

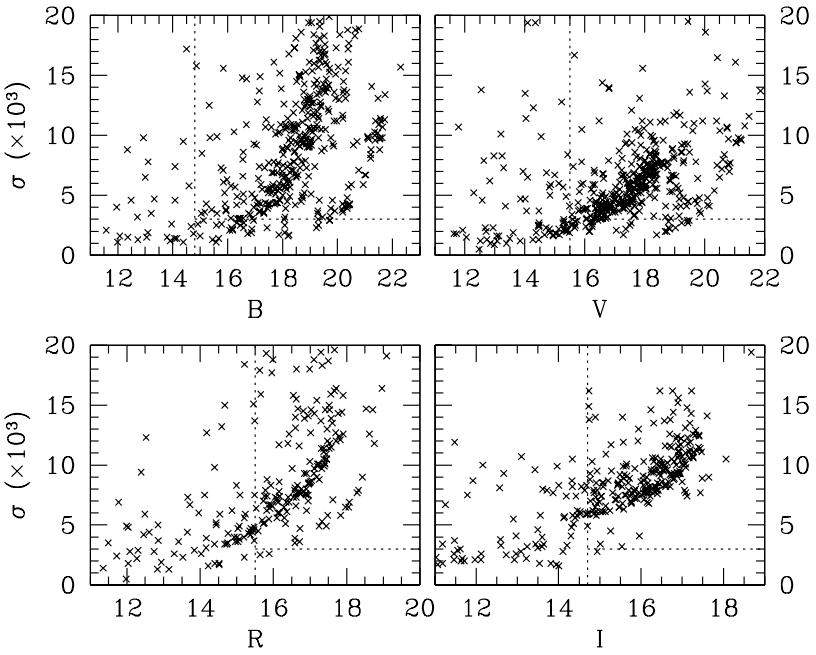

Figure 19: Errors (in milli-magnitudes) reported by Stetson in the four bands of the Stetson standard fields. Also shown (vertical dotted lines) are the "bright magnitude cut-off" limits for 10 second integrations with FORS1.

To answer those questions carefully one would need to place FORS field-size cut-outs on selected standard fields and look at the colours and photometry of the stars of each field. For now we have made a very simple zero-order test of the Stetson fields. We picked (randomly selected to cover RAs evenly) seven of the Stetson fields, and plot in Fig. 19 the errors (in units of milli-magnitude) versus magnitude in the four bands B, V, R and I (Stetson fields report no U band magnitudes). Using the FORS ETC, and assuming grey sky and 0.6 arcsec seeing, we also determined the magnitudes (using the Bessel filters) which would be just below saturation in 10 seconds. Those limits ($B = 14.8, V = 15.5, R = 15.5$ and $I = 14.7$) are also marked in Fig. 19.
It is seen that for the B and the V band the Stetson fields do seem to provide a fair number of standards below the 0.003 mag limit, but for both R and I there is a lack of well determined magnitudes (in our randomly selected sub-set). For U there are no values.

8.5 Future photometry with FORS1 and FORS2

Our tests all suggest that the currently employed method of each night obtaining a new TSI and use those as nightly "Master flats" does not provide the best photometric calibrtaion of the FORSes. We can think of at least two, possibly three, ways that would be better.
One is, as described in Sect. 8.1, to obtain a very deep, high signal-to-noise TSI. Then run through the procedure outlined in this report once only, compute the Master QEF, and use this QEF until it is seen to have changed significantly (e.g. a dust speck has moved). This procedure is only useful if actual changes (e.g. moving dust specks) do not happen too often. If changes are seen nightly, or even weekly, then the recommended strategy would be to "decompose" the QEF into two components, a small scale component (will contain pixel-to-pixel variations and moving dust specks) and a large scale component. During each twilight a new TSI should be obtained, reflecting correctly current positions of dust specks. A simple polynomial fitting routine can then be used to force it onto the correct large scale structure. The large scale structure should be checked at regular intervals in that case.
As briefly mentioned in Sect. 7.2.1 there may be an even simpler strategy, namely to use "flattened" TSI's for calibration. This strategy is a particularly simple case of the second proposal above where one simply forces the large scale component to be completely flat. Such a procedure needs to be carefully tested before it is even considered. The test we did here (Fig. 17, bottom right) suggests that this method could provide some improvement, but the remaining residuals are still quite large so the current evidence does not favour this as the best solution.
As a part of the FAP project a 25 dither point data set was obtained and is currently being analysed. Results from that data set should be able to address this question much better.

8.6 Time and/or rotator angle dependent effects

It has been pointed out several places in this report that there is an outstanding issue with rapidly changing, and in some cases co-rotating with the rotator angle, patterns that cannot be attributed to external effects. The strongest effects are seen in the corners of the CCD, and current evidence leads us to suspect that this is caused either by a variable component of light scattered off mechanical parts that are not stationary with respect to the CCD, or that it is the effect of variable vignetting of the edges of the field. In the first case, scattered light, this will simply be a subcomponent of the TSI, and will be fully corrected for by the method described in this report. In the second case, variable vignetting, the effect is to change QEF during the night. In this case it will be extremely difficult to correct for.
We propose that it must be two of the most important goals of the FAP project to

- Determine the cause of the strong variation in the corners (scattered light or vignetting).

- If the cause is vignetting, then to quantify how strong the effect is as a function of position on the CCD.

With the second question above answered, we would know how much of the corners one would need to ignore in order to get below a certain limit in photometric accuracy.

8.7 Calibration of archived FORS data

The ESO data archive contains a large volume of valuable FORS data. We now ask the question if it is possible to use the method we have developed on archival data. To do this in the "real" sense we would need past sets of rotated and shifted images of the type described in this report. One may search the archive for such data sets, but it is unlikely that enough, or indeed any at all, have been taken. There is an alternative solution though.
For several years it was a part of the calibration plan to obtain both short (typically 1 second) and long (typically 20 seconds) exposures of the Landolt fields. A "limited scope" secondary standard star project would be to determine the relative magnitudes of all stars in the fields observed in the past with long exposures. This would need to be done then only to an accuracy good enough to fit a correction frame F to the past exposures. The combination of old TSI's and correction frames determined from time-identical Landolt field exposures would make it possible to reverse engineer the process and calculate past QEF's. With the production of optimal QEF's for all past exposures it would be interesting to also explore the possibility of making an "on the fly calibration" interface to the archived FORS imaging data.

8.8 Fizz-wig recommendations

Here we list, in order of priority, our recommendations.

- **New master calibration procedure.** We propose to investigate the feasibility of replacing the current "Twilight sky flat fielding" with one of the two schemes we describe in Sect. 8.5.

- **Tracking large and small scale variations of QEF.** We recommend development of a simple automatic procedure for tracking the time evolution of both large scale and small scale variations of the QEF.

- **Identify causes for short term variability.** As mentioned several places in the report, we see evidence for short term variability, notably in the corners of the CCD. This could be due to either variable vignetting (which is effectively impossibly to correct for unless one understands the exact cause), or to a variable scattered component.

- **Limited scope SSP for archived data.** We propose to investigate the feasibility of carrying out a limited scope secondary standard star project aimed at a "reverse engineering" production of past QEF's for the purpose of optimal reduction of archived FORS imaging data (see Sect 8.7). Since

only accurate relative calibration is important here such a project would not need to be linked accurately to the Landolt zero-points, so the VLT could be used for it. We still believe that a more reasonable choice would be the Danish 1.5m telescope (of which ESO has 6 months per year which are currently not being used).

- **Code in CPL for general use.** The method we describe, and therefore the code we have developed, is not specific to FORS but is generically applicable to all CCD imagers. We would be happy to offer the algorithmic parts of it for inclusion into the general scheme of ESO data analysis software, the CPL.

- **On the Fly calibrations.** With our proposed new strategy for definition of QEF's, rather than the direct application of TSI's, we believe that an "on the fly calibration" front-end to the archived FORS imaging data would be a useful and extremely valuable addition to the archive. In case the "limited scope SSP" is carried out this service could even be offered for past data.

- **Full SSP with 1.5mD.** We have demonstrated (Sect. 8.3) that such a project is indeed feasible. We have developed all the methods and tools to carry it out. We have concluded that it is not feasible to do it solely on FORS, but it could be carried out either on a smaller telescope alone, or on a smaller telescope and FORS in combination. The smaller telescope is needed to provide the link to the Landolt zero-points. Before a final decision to start this project, the questions asked in Sect. 8.4 should be addressed. In case it is decided to carry out the project our recommendation is to do it on a smaller telescope. ESO has presently control over the Danish 1.5m telescope for 6 months per year. This would provide ample time to complete the observational part of such a project. A significant amount of work would be going into the data reduction, but no significant development will be required as the software side is ready now. It would be very advisable to take contact to the groups currently undertaking similar projects, at minimum to avoid duplication of efforts, but it may well turn out that they could be interested in a joint project.

References

Andersen, M. I., Freyhammer, L. and Storm, J. (1995). Gain calibration of array detectors by shifted and rotated exposures. In *Calibrating and Understanding HST and ESO Instruments*, European Southern Observatory, ed. Piero Benvenuti, p.87.

Chromey, F. R. and Hasselbacher, D. A. (1996). The Flat Sky: Calibration and Background Uniformity in Wide Field Astronomical Images PASP, **108**, 944.

Dravins, D., Lindegren, L., Mezey, E., Young, A. T., (1998). Atmospheric Intensity Scintillation of Stars. III. Effects for Different Telescope Apertures. PASP, **110**, 610. Equation 10.

Koch, A., Odenkirchen, M., Grebel, E. K., Caldwell, J. A. R. (2003). A calibration map for Wide Field Imager photometry. Astronomische Nachrichten Supplement, **324**, 95.

Landolt, A. U. (1992). UBVRI Photometric standard stars in the magnitude range $11.5 \leq V \leq 16.0$ around the celestial equator. AJ, **104 (1)**, 340.

Mignani, R. and Petr–Gotzens, M. (2005). Measure of the stability of the skyflats in FORS1.

Patat, F. (2003). A robust algorithm for sky background computation in CCD images. A&A, **401**, 797-807.

Patat, F. and Romaniello, M. (2005). Shutter Delay map for FORS1.

Press, W.M., Flannery, B.P., Teukolsky, S.A., & Vetterling, W.T. (1986). Numerical recipes: The art of scientific computing. New York, NY: Cambridge University Press

Saha, A., Dolphin, A. E., Thim, F. (2005). Faint BVRI Photometric Sequences in Selected Fields. PASP, **117**, 37-78.

Schaefer, B. E. (1998). To the Visual Limits. S&T, May, p57.

Stetson, P. B. (2000). Homogeneous Photometry for Star Clusters and Resolved Galaxies. II Photometric Standard Stars. PASP, **112**, 925-931.

Vandame, B. (2004). Traitement d'images a Grand-Champs et multi-longeurs d'ondes. Application aux releves "ESO Imaging Survey". PhD thesis, Universite de Nice.

Young, A. T. (1967). Photometric error analysis. VI. Confirmation of Reiger's theory of scintillation. AJ, **72**, 747.

A Resolution of FORS-IOT action item AI03-5

Present draft plan for "Faint Photometric Standards for VLT" project.

Palle Moller

24.07.03

Summary

This document represents the resolution of my FORS IOT Action Item. I here present a plan for the definition of a network of dedicated VLT photometric standard fields. The individual steps to be taken are described in some detail. An approximate timeline, and a rough overview of the amount of resources needed (observing time, archived data, and data reduction and analysis) is given.

1 Background

The wish to set up a network of dedicated VLT photometric standard fields has been with us since the very beginning of VLT operations, and even before that. For several periods FORS was (is still?) collecting data with this purpose in mind, but nothing has happened with the data so far. There are two main reasons for this:

a) Various problems with FORS has made it unclear how one can obtain the necessary (about 0.001 mag) photometric errors.

b) No individual on the FORS IOT has enough time to take on this task.

In order to move forward with this project, the completion of which is still seen by the FORS IOT as an important step for the VLT calibration plan, an action item was assigned to formulate a plan. The action item resulted in this document.

2 Resolving technical issues

There were originally two technical issues: The time variability of the FORS QE and flatfielding. The first of those issues is now under control to a point where we need not worry about it, the second is still unresolved. To resolve it we would need to obtain a series of test exposures with FORS 1. Those exposures can almost all be obtained during twilight. What we need is effectively FFs for several filters taken with different rotator positions and different positions of the guide probe. In addition a standard star field should be observed also

with different rotator positions and different positions of the guide probe. A few additional short night-time exposures should be taken to verify the results.

Analysis of such a data set will allow us to define the actual strategy needed to carry out the "Faint Photometric Standards for VLT" project. The time needed for this analysis I estimate at roughly 1 full 40 hour week. I propose that we ask the office for science to allocate a Garching fellow to complete this part of the pre-study.

3 The project

The project proper has several steps in it, and what is given below is merely a summary of those. This is all known technology so there are no "unknowns" in the project, only some decisions concerning which data collection strategy is the most efficient for the observatory. For example we could continue with the previous plan to execute the project slowly "step-by-step" adding extra exposures during the daily std field observations, or we could request a few full photometric nights to the project, and get it done quickly and efficiently at the cost of those nights. A good fraction of such observations could be done during the "low pressure" season, so a mix between the two modes is probably the optimal.

The goal is to define a set of std fields (obvious choice is to use Landolt fields), each with a set of stars in the optimal magnitude range for VLT standards, which have no contaminating neighbours, which are not variable, and which evenly map out a full colour sequence.

The existing large database of Landolt field observations is good enough for calibration to within 5%, and since we have a long baseline to check against variability it is perfect for the selection of those objects. The data are most likely not, however, good enough for the actual photometry.

a) The first task is therefore to reduce those data, select good candidates, check for variability, and make a final list.

b) The second task is then to obtain high precision photometric data of all the objects in this final list.

c) Basic reductions of this set of data will have to proceed then as defined during the first part of the project (section 2). It may well be worth while to create a special "high precision" pipeline for this purpose.

d) Photometric measurements on the reduced frames should use the most recent high precision techniques. Error bars on milli-magnitude scale are now routinely obtained for studies of e.g. stellar oscillations. We should invite an expert on those techniques to visit as part of the visitor programme to share their expertise.

e) Final interpretation of the data involves decomposing the data into object magnitudes/colours, VLT/FORS instrumental system colour terms, and Paranal extinction terms. Since the goal is to effectively "enlarge" the Landolt fields, inviting Landolt under the ESO visitor programme may provide valuable insight.

As a bi-product of the above we will determine with high accuracy the extinction curve at Paranal and the colour terms of the FORS photometric system. An additional bi-product is a well defined procedure for accurate FORS photometry which can then be offered to our users and incorporated into the FORS pipeline.

The project requires a dedicated full time PA or similar for a period of about 1 year. The pre-study (section 2) should be completed in the fall of 2003. The person to do the larger part of this project should be hired for 2004.

B Observing Log

All observations and calibrations discussed in this report were obtained with FORS1 on March 26-27, 2004. Details of the observations, including archive filenames for easy reference, are provided in the lists below.

PROG_ID: 60.A-9203(A), DPR_CATG: CALIB, DPR_TECH: IMAGE, CONAD: 1.46, CLOCK: ABCD, BIN: 1x1, WINDOWS: 2080x2048

TARGET	T#	TPL_ID	NX	X#	archive_filename	origfilename	DPR_TYPE	FILTER	AIRM	EXP
twil-0427	3	img_cal_skyf	8	4	FORS1.2004-03-26T23:13:15.381.fits	IMG_CALSKY086.8.fits	FLAT,SKY	B_BESS	1.18	2.30
twil-0427	3	img_cal_skyf	8	5	FORS1.2004-03-26T23:14:06.236.fits	IMG_CALSKY086.9.fits	FLAT,SKY	B_BESS	1.18	3.84
twil-0427	3	img_cal_skyf	8	6	FORS1.2004-03-26T23:14:58.572.fits	IMG_CALSKY086.10.fits	FLAT,SKY	B_BESS	1.18	4.90
twil-0427	3	img_cal_skyf	8	7	FORS1.2004-03-26T23:15:52.147.fits	IMG_CALSKY086.11.fits	FLAT,SKY	B_BESS	1.19	6.24
twil-0427	3	img_cal_skyf	6	2	FORS1.2004-03-26T23:23:23.173.fits	IMG_CALSKY086.18.fits	FLAT,SKY	B_BESS	1.21	11.8
twil-0427	3	img_cal_skyf	6	3	FORS1.2004-03-26T23:24:25.069.fits	IMG_CALSKY086.19.fits	FLAT,SKY	B_BESS	1.21	62.4
twil-0427	3	img_cal_skyf	6	4	FORS1.2004-03-26T23:26:16.750.fits	IMG_CALSKY086.20.fits	FLAT,SKY	B_BESS	1.21	86.3
twil-0427	3	img_cal_skyf	6	5	FORS1.2004-03-26T23:28:33.073.fits	IMG_CALSKY086.21.fits	FLAT,SKY	B_BESS	1.22	139.
twil-0427	6	img_cal_skyf	9	2	FORS1.2004-03-26T23:32:51.478.fits	IMG_CALSKY086.23.fits	FLAT,SKY	R_BESS	1.24	13.1
twil-0427	6	img_cal_skyf	9	3	FORS1.2004-03-26T23:33:54.575.fits	IMG_CALSKY086.24.fits	FLAT,SKY	R_BESS	1.24	190.
galactic-airpl	2	img_obs_crsp	1	1	FORS1.2004-03-27T00:16:39.161.fits	IMG_STD087.fits	STD	B_BESS	1.22	4.99
galactic-airpl	3	img_obs_crsp	1	1	FORS1.2004-03-27T00:17:52.508.fits	IMG_STD087.1.fits	STD	R_BESS	1.22	1.99
galactic-airpl	2	img_obs_crsp	1	1	FORS1.2004-03-27T00:20:14.992.fits	IMG_STD087.2.fits	STD	B_BESS	1.22	4.99
galactic-airpl	3	img_obs_crsp	1	1	FORS1.2004-03-27T00:21:28.100.fits	IMG_STD087.3.fits	STD	R_BESS	1.22	1.99
galactic-airpl	2	img_obs_crsp	1	1	FORS1.2004-03-27T00:24:05.235.fits	IMG_STD087.4.fits	STD	B_BESS	1.22	4.99
galactic-airpl	3	img_obs_crsp	1	1	FORS1.2004-03-27T00:25:18.483.fits	IMG_STD087.5.fits	STD	R_BESS	1.22	1.99
galactic-airpl	2	img_obs_crsp	5	1	FORS1.2004-03-27T00:27:31.666.fits	IMG_STD087.6.fits	STD	B_BESS	1.22	4.99
galactic-airpl	2	img_obs_crsp	5	1	FORS1.2004-03-27T00:34:18.504.fits	IMG_STD087.7.fits	STD	B_BESS	1.22	4.98
galactic-airpl	2	img_obs_crsp	5	2	FORS1.2004-03-27T00:35:21.441.fits	IMG_STD087.8.fits	STD	B_BESS	1.22	4.99
galactic-airpl	2	img_obs_crsp	5	1	FORS1.2004-03-27T00:45:21.260.fits	IMG_STD087.9.fits	STD	B_BESS	1.23	4.99
galactic-airpl	2	img_obs_crsp	5	2	FORS1.2004-03-27T00:46:25.086.fits	IMG_STD087.10.fits	STD	B_BESS	1.23	5.00
galactic-airpl	2	img_obs_crsp	3	1	FORS1.2004-03-27T00:52:30.953.fits	IMG_STD087.11.fits	STD	B_BESS	1.23	4.99
galactic-airpl	2	img_obs_crsp	3	2	FORS1.2004-03-27T00:55:48.522.fits	IMG_STD087.12.fits	STD	B_BESS	1.23	4.99
galactic-airpl	2	img_obs_crsp	3	3	FORS1.2004-03-27T00:57:15.241.fits	IMG_STD087.13.fits	STD	B_BESS	1.23	5.00
galactic-airpl	3	img_obs_crsp	5	1	FORS1.2004-03-27T01:01:54.218.fits	IMG_STD087.14.fits	STD	R_BESS	1.23	1.99
galactic-airpl	3	img_obs_crsp	4	1	FORS1.2004-03-27T01:04:05.409.fits	IMG_STD087.15.fits	STD	R_BESS	1.23	1.99
galactic-airpl	3	img_obs_crsp	4	2	FORS1.2004-03-27T01:07:30.019.fits	IMG_STD087.16.fits	STD	R_BESS	1.24	1.99
galactic-airpl	2	img_obs_crsp	5	1	FORS1.2004-03-27T01:18:23.244.fits	IMG_STD087.17.fits	STD	B_BESS	1.24	5.00
galactic-airpl	2	img_obs_crsp	4	1	FORS1.2004-03-27T01:22:22.818.fits	IMG_STD087.18.fits	STD	B_BESS	1.25	5.00
galactic-airpl	2	img_obs_crsp	4	2	FORS1.2004-03-27T01:24:10.958.fits	IMG_STD087.19.fits	STD	B_BESS	1.25	4.99
galactic-airpl	2	img_obs_crsp	2	1	FORS1.2004-03-27T01:32:58.680.fits	IMG_STD087.20.fits	STD	B_BESS	1.26	5.00
galactic-airpl	2	img_obs_crsp	1	1	FORS1.2004-03-27T01:35:42.506.fits	IMG_STD087.21.fits	STD	B_BESS	1.26	5.00
galactic-airpl	3	img_obs_crsp	5	1	FORS1.2004-03-27T01:40:30.173.fits	IMG_STD087.22.fits	STD	R_BESS	1.26	1.99
galactic-airpl	3	img_obs_crsp	4	1	FORS1.2004-03-27T01:42:38.086.fits	IMG_STD087.23.fits	STD	R_BESS	1.26	2.00
galactic-airpl	3	img_obs_crsp	4	2	FORS1.2004-03-27T01:44:47.159.fits	IMG_STD087.24.fits	STD	R_BESS	1.27	1.99
galactic-airpl	3	img_obs_crsp	2	1	FORS1.2004-03-27T01:48:48.273.fits	IMG_STD087.25.fits	STD	R_BESS	1.27	2.00
galactic-airpl	3	img_obs_crsp	1	1	FORS1.2004-03-27T01:50:22.011.fits	IMG_STD087.26.fits	STD	R_BESS	1.27	1.99
galactic-airpl	4	img_obs_crsp	5	1	FORS1.2004-03-27T01:54:03.644.fits	IMG_STD087.27.fits	STD	R_BESS	1.28	1.00
galactic-airpl	4	img_obs_crsp	5	2	FORS1.2004-03-27T01:54:52.776.fits	IMG_STD087.28.fits	STD	R_BESS	1.28	1.00
galactic-airpl	4	img_obs_crsp	5	3	FORS1.2004-03-27T01:55:41.450.fits	IMG_STD087.29.fits	STD	R_BESS	1.28	0.99
galactic-airpl	4	img_obs_crsp	5	4	FORS1.2004-03-27T01:56:30.316.fits	IMG_STD087.30.fits	STD	R_BESS	1.28	0.99
galactic-airpl	4	img_obs_crsp	5	5	FORS1.2004-03-27T01:57:19.630.fits	IMG_STD087.31.fits	STD	R_BESS	1.28	1.00
galactic-airpl	4	img_obs_crsp	4	1	FORS1.2004-03-27T01:59:59.396.fits	IMG_STD087.32.fits	STD	R_BESS	1.29	0.99
galactic-airpl	4	img_obs_crsp	4	2	FORS1.2004-03-27T02:01:37.176.fits	IMG_STD087.33.fits	STD	R_BESS	1.29	1.00
galactic-airpl	4	img_obs_crsp	4	3	FORS1.2004-03-27T02:03:56.549.fits	IMG_STD087.34.fits	STD	R_BESS	1.29	0.98
galactic-airpl	4	img_obs_crsp	1	1	FORS1.2004-03-27T02:07:31.561.fits	IMG_STD087.35.fits	STD	R_BESS	1.30	0.99
twil-1802	3	img_cal_skyf	12	5	FORS1.2004-03-27T10:06:20.625.fits	IMG_CALSKY087.4.fits	FLAT,SKY	R_BESS	1.06	81.2
twil-1802	3	img_cal_skyf	12	6	FORS1.2004-03-27T10:08:30.628.fits	IMG_CALSKY087.5.fits	FLAT,SKY	R_BESS	1.06	59.1
twil-1802	3	img_cal_skyf	12	7	FORS1.2004-03-27T10:10:19.498.fits	IMG_CALSKY087.6.fits	FLAT,SKY	R_BESS	1.06	46.2
twil-1802	3	img_cal_skyf	12	8	FORS1.2004-03-27T10:11:54.228.fits	IMG_CALSKY087.7.fits	FLAT,SKY	R_BESS	1.06	36.8
twil-1802	3	img_cal_skyf	12	9	FORS1.2004-03-27T10:13:19.896.fits	IMG_CALSKY087.8.fits	FLAT,SKY	R_BESS	1.06	30.4
twil-1802	3	img_cal_skyf	12	10	FORS1.2004-03-27T10:14:39.754.fits	IMG_CALSKY087.9.fits	FLAT,SKY	R_BESS	1.06	23.4
twil-1802	3	img_cal_skyf	12	11	FORS1.2004-03-27T10:15:51.441.fits	IMG_CALSKY087.10.fits	FLAT,SKY	R_BESS	1.06	17.9

PROG_ID: 60.A-9203(C), DPR_CATG: CALIB, DPR_TECH: IMAGE, CONAD: 1.46, CLOCK: ABCD, BIN: 1x1, WINDOWS: 2080x2048

TARGET	T#	TPL_ID	NX	X#	archive_filename	origfilename	DPR_TYPE	FILTER	AIRM	EXP
****	1	img_cal_bias	5	1	FORS1.2004-03-26T13:17:53.643.fits	IMG_CAL086.38.fits	BIAS	****	-99	0.06
****	1	img_cal_bias	5	2	FORS1.2004-03-26T13:18:37.567.fits	IMG_CAL086.39.fits	BIAS	****	-99	0.06
****	1	img_cal_bias	5	3	FORS1.2004-03-26T13:19:21.552.fits	IMG_CAL086.40.fits	BIAS	****	-99	0.06
****	1	img_cal_bias	5	4	FORS1.2004-03-26T13:20:05.646.fits	IMG_CAL086.41.fits	BIAS	****	-99	0.06
****	1	img_cal_bias	5	5	FORS1.2004-03-26T13:20:49.650.fits	IMG_CAL086.42.fits	BIAS	****	-99	0.06
****	2	img_cal_bias	5	1	FORS1.2004-03-26T13:28:36.665.fits	IMG_CAL086.43.fits	BIAS	****	-99	0.06
****	2	img_cal_bias	5	2	FORS1.2004-03-26T13:29:20.719.fits	IMG_CAL086.44.fits	BIAS	****	-99	0.06
****	2	img_cal_bias	5	3	FORS1.2004-03-26T13:30:04.854.fits	IMG_CAL086.45.fits	BIAS	****	-99	0.06
****	2	img_cal_bias	5	4	FORS1.2004-03-26T13:30:48.838.fits	IMG_CAL086.46.fits	BIAS	****	-99	0.06
****	2	img_cal_bias	5	5	FORS1.2004-03-26T13:31:32.863.fits	IMG_CAL086.47.fits	BIAS	****	-99	0.06
****	3	img_cal_bias	5	1	FORS1.2004-03-26T13:39:50.111.fits	IMG_CAL086.48.fits	BIAS	****	-99	0.06
****	3	img_cal_bias	5	2	FORS1.2004-03-26T13:40:34.116.fits	IMG_CAL086.49.fits	BIAS	****	-99	0.06
****	3	img_cal_bias	5	3	FORS1.2004-03-26T13:41:18.192.fits	IMG_CAL086.50.fits	BIAS	****	-99	0.06
****	3	img_cal_bias	5	4	FORS1.2004-03-26T13:42:02.246.fits	IMG_CAL086.51.fits	BIAS	****	-99	0.06
****	3	img_cal_bias	5	5	FORS1.2004-03-26T13:42:46.371.fits	IMG_CAL086.52.fits	BIAS	****	-99	0.06
****	4	img_cal_bias	5	1	FORS1.2004-03-26T14:00:57.419.fits	IMG_CAL086.53.fits	BIAS	****	-99	0.06
****	4	img_cal_bias	5	2	FORS1.2004-03-26T14:01:41.274.fits	IMG_CAL086.54.fits	BIAS	****	-99	0.06
****	4	img_cal_bias	5	3	FORS1.2004-03-26T14:02:25.539.fits	IMG_CAL086.55.fits	BIAS	****	-99	0.06
****	4	img_cal_bias	5	4	FORS1.2004-03-26T14:03:09.983.fits	IMG_CAL086.56.fits	BIAS	****	-99	0.06
****	4	img_cal_bias	5	5	FORS1.2004-03-26T14:03:54.387.fits	IMG_CAL086.57.fits	BIAS	****	-99	0.06
****	5	img_cal_bias	5	1	FORS1.2004-03-26T14:09:51.602.fits	IMG_CAL086.58.fits	BIAS	****	-99	0.06
****	5	img_cal_bias	5	2	FORS1.2004-03-26T14:10:35.947.fits	IMG_CAL086.59.fits	BIAS	****	-99	0.06
****	5	img_cal_bias	5	3	FORS1.2004-03-26T14:11:20.331.fits	IMG_CAL086.60.fits	BIAS	****	-99	0.06
****	5	img_cal_bias	5	4	FORS1.2004-03-26T14:12:04.785.fits	IMG_CAL086.61.fits	BIAS	****	-99	0.06
****	5	img_cal_bias	5	5	FORS1.2004-03-26T14:12:49.010.fits	IMG_CAL086.62.fits	BIAS	****	-99	0.06
****	6	img_cal_bias	5	1	FORS1.2004-03-26T14:20:26.255.fits	IMG_CAL086.63.fits	BIAS	****	-99	0.06
****	6	img_cal_bias	5	2	FORS1.2004-03-26T14:21:10.469.fits	IMG_CAL086.64.fits	BIAS	****	-99	0.06
****	6	img_cal_bias	5	3	FORS1.2004-03-26T14:21:54.754.fits	IMG_CAL086.65.fits	BIAS	****	-99	0.06
****	6	img_cal_bias	5	4	FORS1.2004-03-26T14:22:39.068.fits	IMG_CAL086.66.fits	BIAS	****	-99	0.06
****	6	img_cal_bias	5	5	FORS1.2004-03-26T14:23:23.382.fits	IMG_CAL086.67.fits	BIAS	****	-99	0.06
****	7	img_cal_bias	5	1	FORS1.2004-03-26T14:29:22.198.fits	IMG_CAL086.68.fits	BIAS	****	-99	0.06
****	7	img_cal_bias	5	2	FORS1.2004-03-26T14:30:06.512.fits	IMG_CAL086.69.fits	BIAS	****	-99	0.06
****	7	img_cal_bias	5	3	FORS1.2004-03-26T14:30:50.646.fits	IMG_CAL086.70.fits	BIAS	****	-99	0.06
****	7	img_cal_bias	5	4	FORS1.2004-03-26T14:31:34.891.fits	IMG_CAL086.71.fits	BIAS	****	-99	0.06
****	7	img_cal_bias	5	5	FORS1.2004-03-26T14:32:19.096.fits	IMG_CAL086.72.fits	BIAS	****	-99	0.06
****	8	img_cal_bias	5	1	FORS1.2004-03-26T14:43:01.398.fits	IMG_CAL086.73.fits	BIAS	****	-99	0.06
****	8	img_cal_bias	5	2	FORS1.2004-03-26T14:43:45.883.fits	IMG_CAL086.74.fits	BIAS	****	-99	0.06
****	8	img_cal_bias	5	3	FORS1.2004-03-26T14:44:30.238.fits	IMG_CAL086.75.fits	BIAS	****	-99	0.06
****	8	img_cal_bias	5	4	FORS1.2004-03-26T14:45:14.402.fits	IMG_CAL086.76.fits	BIAS	****	-99	0.06
****	8	img_cal_bias	5	5	FORS1.2004-03-26T14:45:58.756.fits	IMG_CAL086.77.fits	BIAS	****	-99	0.06
****	9	img_cal_bias	5	1	FORS1.2004-03-26T14:51:03.707.fits	IMG_CAL086.78.fits	BIAS	****	-99	0.06
****	9	img_cal_bias	5	2	FORS1.2004-03-26T14:51:48.122.fits	IMG_CAL086.79.fits	BIAS	****	-99	0.06
****	9	img_cal_bias	5	3	FORS1.2004-03-26T14:52:32.466.fits	IMG_CAL086.80.fits	BIAS	****	-99	0.06
****	9	img_cal_bias	5	4	FORS1.2004-03-26T14:53:16.910.fits	IMG_CAL086.81.fits	BIAS	****	-99	0.06
****	9	img_cal_bias	5	5	FORS1.2004-03-26T14:54:01.085.fits	IMG_CAL086.82.fits	BIAS	****	-99	0.06
****	10	img_cal_bias	5	1	FORS1.2004-03-26T15:08:39.782.fits	IMG_CAL086.83.fits	BIAS	****	-99	0.06
****	10	img_cal_bias	5	2	FORS1.2004-03-26T15:09:23.996.fits	IMG_CAL086.84.fits	BIAS	****	-99	0.06
****	10	img_cal_bias	5	3	FORS1.2004-03-26T15:10:08.260.fits	IMG_CAL086.85.fits	BIAS	****	-99	0.06
****	10	img_cal_bias	5	4	FORS1.2004-03-26T15:10:52.525.fits	IMG_CAL086.86.fits	BIAS	****	-99	0.06
****	10	img_cal_bias	5	5	FORS1.2004-03-26T15:11:36.929.fits	IMG_CAL086.87.fits	BIAS	****	-99	0.06
****	11	img_cal_bias	5	1	FORS1.2004-03-26T15:27:45.092.fits	IMG_CAL086.88.fits	BIAS	****	-99	0.06
****	11	img_cal_bias	5	2	FORS1.2004-03-26T15:28:29.387.fits	IMG_CAL086.89.fits	BIAS	****	-99	0.06
****	11	img_cal_bias	5	3	FORS1.2004-03-26T15:29:13.542.fits	IMG_CAL086.90.fits	BIAS	****	-99	0.06

PROG_ID: 60.A-9203(C), DPR_CATG: CALIB, DPR_TECH: IMAGE, CONAD: 1.46, CLOCK: ABCD, BIN: 1x1, WINDOWS: 2080x2048

TARGET	T#	TPL_ID	NX	X#	archive_filename	origfilename	DPR_TYPE	FILTER	AIRM	EXP
****	11	img_ca|_bias	5	4	FORS1.2004-03-26T15:29:57.955.fits	IMG_CAL086.91.fits	BIAS	****	-99	0.06
****	11	img_ca|_bias	5	5	FORS1.2004-03-26T15:30:42.480.fits	IMG_CAL086.92.fits	BIAS	****	-99	0.06
****	12	img_ca|_bias	5	1	FORS1.2004-03-26T15:43:12.627.fits	IMG_CAL086.93.fits	BIAS	****	-99	0.06
****	12	img_ca|_bias	5	2	FORS1.2004-03-26T15:43:56.921.fits	IMG_CAL086.94.fits	BIAS	****	-99	0.06
****	12	img_ca|_bias	5	3	FORS1.2004-03-26T15:44:41.105.fits	IMG_CAL086.95.fits	BIAS	****	-99	0.06
****	12	img_ca|_bias	5	4	FORS1.2004-03-26T15:45:25.360.fits	IMG_CAL086.96.fits	BIAS	****	-99	0.06
****	12	img_ca|_bias	5	5	FORS1.2004-03-26T15:46:09.695.fits	IMG_CAL086.97.fits	BIAS	****	-99	0.06
****	13	img_ca|_bias	5	1	FORS1.2004-03-26T15:53:32.818.fits	IMG_CAL086.98.fits	BIAS	****	-99	0.06
****	13	img_ca|_bias	5	2	FORS1.2004-03-26T15:54:17.032.fits	IMG_CAL086.99.fits	BIAS	****	-99	0.06
****	13	img_ca|_bias	5	3	FORS1.2004-03-26T15:55:01.357.fits	IMG_CAL086.100.fits	BIAS	****	-99	0.06
****	13	img_ca|_bias	5	4	FORS1.2004-03-26T15:55:45.831.fits	IMG_CAL086.101.fits	BIAS	****	-99	0.06
****	13	img_ca|_bias	5	5	FORS1.2004-03-26T15:56:30.365.fits	IMG_CAL086.102.fits	BIAS	****	-99	0.06
****	14	img_ca|_bias	5	1	FORS1.2004-03-26T16:13:41.009.fits	IMG_CAL086.103.fits	BIAS	****	-99	0.06
****	14	img_ca|_bias	5	2	FORS1.2004-03-26T16:14:25.352.fits	IMG_CAL086.104.fits	BIAS	****	-99	0.06
****	14	img_ca|_bias	5	3	FORS1.2004-03-26T16:15:09.547.fits	IMG_CAL086.105.fits	BIAS	****	-99	0.06
****	14	img_ca|_bias	5	4	FORS1.2004-03-26T16:15:53.871.fits	IMG_CAL086.106.fits	BIAS	****	-99	0.06
****	14	img_ca|_bias	5	5	FORS1.2004-03-26T16:16:38.085.fits	IMG_CAL086.107.fits	BIAS	****	-99	0.06
****	15	img_ca|_bias	5	1	FORS1.2004-03-26T16:22:04.768.fits	IMG_CAL086.108.fits	BIAS	****	-99	0.06
****	15	img_ca|_bias	5	2	FORS1.2004-03-26T16:22:49.242.fits	IMG_CAL086.109.fits	BIAS	****	-99	0.06
****	15	img_ca|_bias	5	3	FORS1.2004-03-26T16:23:33.566.fits	IMG_CAL086.110.fits	BIAS	****	-99	0.06
****	15	img_ca|_bias	5	4	FORS1.2004-03-26T16:24:18.021.fits	IMG_CAL086.111.fits	BIAS	****	-99	0.06
****	15	img_ca|_bias	5	5	FORS1.2004-03-26T16:25:02.395.fits	IMG_CAL086.112.fits	BIAS	****	-99	0.06
****	16	img_ca|_bias	5	1	FORS1.2004-03-26T17:00:34.027.fits	IMG_CAL086.113.fits	BIAS	****	-99	0.06
****	16	img_ca|_bias	5	2	FORS1.2004-03-26T17:01:18.301.fits	IMG_CAL086.114.fits	BIAS	****	-99	0.06
****	16	img_ca|_bias	5	3	FORS1.2004-03-26T17:02:02.425.fits	IMG_CAL086.115.fits	BIAS	****	-99	0.06
****	16	img_ca|_bias	5	4	FORS1.2004-03-26T17:02:46.700.fits	IMG_CAL086.116.fits	BIAS	****	-99	0.06
****	16	img_ca|_bias	5	5	FORS1.2004-03-26T17:03:31.135.fits	IMG_CAL086.117.fits	BIAS	****	-99	0.06
****	17	img_ca|_bias	5	1	FORS1.2004-03-26T17:19:04.077.fits	IMG_CAL086.118.fits	BIAS	****	-99	0.06
****	17	img_ca|_bias	5	2	FORS1.2004-03-26T17:19:48.350.fits	IMG_CAL086.119.fits	BIAS	****	-99	0.06
****	17	img_ca|_bias	5	3	FORS1.2004-03-26T17:20:32.565.fits	IMG_CAL086.120.fits	BIAS	****	-99	0.06
****	17	img_ca|_bias	5	4	FORS1.2004-03-26T17:21:17.079.fits	IMG_CAL086.121.fits	BIAS	****	-99	0.06
****	17	img_ca|_bias	5	5	FORS1.2004-03-26T17:22:01.354.fits	IMG_CAL086.122.fits	BIAS	****	-99	0.06
****	18	img_ca|_bias	5	1	FORS1.2004-03-26T17:34:17.636.fits	IMG_CAL086.123.fits	BIAS	****	-99	0.06
****	18	img_ca|_bias	5	2	FORS1.2004-03-26T17:35:02.091.fits	IMG_CAL086.124.fits	BIAS	****	-99	0.06
****	18	img_ca|_bias	5	3	FORS1.2004-03-26T17:35:46.365.fits	IMG_CAL086.125.fits	BIAS	****	-99	0.06
****	18	img_ca|_bias	5	4	FORS1.2004-03-26T17:36:30.640.fits	IMG_CAL086.126.fits	BIAS	****	-99	0.06
****	18	img_ca|_bias	5	5	FORS1.2004-03-26T17:37:14.973.fits	IMG_CAL086.127.fits	BIAS	****	-99	0.06
****	19	img_ca|_bias	5	1	FORS1.2004-03-26T18:19:59.839.fits	IMG_CAL086.128.fits	BIAS	****	-99	0.06
****	19	img_ca|_bias	5	2	FORS1.2004-03-26T18:20:44.053.fits	IMG_CAL086.129.fits	BIAS	****	-99	0.06
****	19	img_ca|_bias	5	3	FORS1.2004-03-26T18:21:28.207.fits	IMG_CAL086.130.fits	BIAS	****	-99	0.06
****	19	img_ca|_bias	5	4	FORS1.2004-03-26T18:22:12.631.fits	IMG_CAL086.131.fits	BIAS	****	-99	0.06
****	19	img_ca|_bias	5	5	FORS1.2004-03-26T18:22:56.926.fits	IMG_CAL086.132.fits	BIAS	****	-99	0.06
****	20	img_ca|_bias	5	1	FORS1.2004-03-26T18:31:04.784.fits	IMG_CAL086.133.fits	BIAS	****	-99	0.06
****	20	img_ca|_bias	5	2	FORS1.2004-03-26T18:31:49.149.fits	IMG_CAL086.134.fits	BIAS	****	-99	0.06
****	20	img_ca|_bias	5	3	FORS1.2004-03-26T18:32:33.203.fits	IMG_CAL086.135.fits	BIAS	****	-99	0.06
****	20	img_ca|_bias	5	4	FORS1.2004-03-26T18:33:17.538.fits	IMG_CAL086.136.fits	BIAS	****	-99	0.06
****	20	img_ca|_bias	5	5	FORS1.2004-03-26T18:34:01.842.fits	IMG_CAL086.137.fits	BIAS	****	-99	0.06
****	21	img_ca|_bias	5	1	FORS1.2004-03-26T18:41:12.404.fits	IMG_CAL086.138.fits	BIAS	****	-99	0.06
****	21	img_ca|_bias	5	2	FORS1.2004-03-26T18:41:56.669.fits	IMG_CAL086.139.fits	BIAS	****	-99	0.06
****	21	img_ca|_bias	5	3	FORS1.2004-03-26T18:42:40.993.fits	IMG_CAL086.140.fits	BIAS	****	-99	0.06
****	21	img_ca|_bias	5	4	FORS1.2004-03-26T18:43:25.367.fits	IMG_CAL086.141.fits	BIAS	****	-99	0.06
****	21	img_ca|_bias	5	5	FORS1.2004-03-26T18:44:09.602.fits	IMG_CAL086.142.fits	BIAS	****	-99	0.06
****	22	img_ca|_bias	5	1	FORS1.2004-03-26T18:54:11.395.fits	IMG_CAL086.143.fits	BIAS	****	-99	0.06

TARGET	T#	TPL_ID	NX	X#	archive_filename	origfilename	DPR_TYPE	FILTER	AIRM	EXP
****	22	img_cal_bias	5	2	FORS1.2004-03-26T18:54:55.800.fits	IMG_CAL086.144.fits	BIAS	****	-99	0.06
****	22	img_cal_bias	5	3	FORS1.2004-03-26T18:55:40.134.fits	IMG_CAL086.145.fits	BIAS	****	-99	0.06
****	22	img_cal_bias	5	4	FORS1.2004-03-26T18:56:24.529.fits	IMG_CAL086.146.fits	BIAS	****	-99	0.04
****	22	img_cal_bias	5	5	FORS1.2004-03-26T18:57:08.803.fits	IMG_CAL086.147.fits	BIAS	****	-99	0.06
****	23	img_cal_bias	5	1	FORS1.2004-03-26T19:08:21.729.fits	IMG_CAL086.148.fits	BIAS	****	-99	0.06
****	23	img_cal_bias	5	2	FORS1.2004-03-26T19:09:05.983.fits	IMG_CAL086.149.fits	BIAS	****	-99	0.06
****	23	img_cal_bias	5	3	FORS1.2004-03-26T19:09:50.178.fits	IMG_CAL086.150.fits	BIAS	****	-99	0.06
****	23	img_cal_bias	5	4	FORS1.2004-03-26T19:10:34.792.fits	IMG_CAL086.151.fits	BIAS	****	-99	0.06
****	23	img_cal_bias	5	5	FORS1.2004-03-26T19:11:19.127.fits	IMG_CAL086.152.fits	BIAS	****	-99	0.06
****	24	img_cal_bias	5	1	FORS1.2004-03-26T19:15:14.371.fits	IMG_CAL086.153.fits	BIAS	****	-99	0.06
****	24	img_cal_bias	5	2	FORS1.2004-03-26T19:15:58.745.fits	IMG_CAL086.154.fits	BIAS	****	-99	0.06
****	24	img_cal_bias	5	3	FORS1.2004-03-26T19:16:43.029.fits	IMG_CAL086.155.fits	BIAS	****	-99	0.06
****	24	img_cal_bias	5	4	FORS1.2004-03-26T19:17:27.504.fits	IMG_CAL086.156.fits	BIAS	****	-99	0.06
****	24	img_cal_bias	5	5	FORS1.2004-03-26T19:18:11.888.fits	IMG_CAL086.157.fits	BIAS	****	-99	0.06
****	25	img_cal_bias	5	1	FORS1.2004-03-26T19:26:45.155.fits	IMG_CAL086.158.fits	BIAS	****	-99	0.04
****	25	img_cal_bias	5	2	FORS1.2004-03-26T19:27:29.350.fits	IMG_CAL086.159.fits	BIAS	****	-99	0.06
****	25	img_cal_bias	5	3	FORS1.2004-03-26T19:28:13.664.fits	IMG_CAL086.160.fits	BIAS	****	-99	0.06
****	25	img_cal_bias	5	4	FORS1.2004-03-26T19:28:58.148.fits	IMG_CAL086.161.fits	BIAS	****	-99	0.06
****	25	img_cal_bias	5	5	FORS1.2004-03-26T19:29:42.552.fits	IMG_CAL086.162.fits	BIAS	****	-99	0.06
****	1	img_cal_bias	5	1	FORS1.2004-03-26T19:32:10.877.fits	IMG_CAL086.163.fits	BIAS	****	-99	0.06
****	1	img_cal_bias	5	2	FORS1.2004-03-26T19:32:55.211.fits	IMG_CAL086.164.fits	BIAS	****	-99	0.06
****	1	img_cal_bias	5	3	FORS1.2004-03-26T19:33:39.566.fits	IMG_CAL086.165.fits	BIAS	****	-99	0.06
****	1	img_cal_bias	5	4	FORS1.2004-03-26T19:34:23.760.fits	IMG_CAL086.166.fits	BIAS	****	-99	0.06
****	1	img_cal_bias	5	5	FORS1.2004-03-26T19:35:08.025.fits	IMG_CAL086.167.fits	BIAS	****	-99	0.06
****	2	img_cal_bias	5	1	FORS1.2004-03-26T19:44:11.571.fits	IMG_CAL086.168.fits	BIAS	****	-99	0.06
****	2	img_cal_bias	5	2	FORS1.2004-03-26T19:44:55.905.fits	IMG_CAL086.169.fits	BIAS	****	-99	0.06
****	2	img_cal_bias	5	3	FORS1.2004-03-26T19:45:40.150.fits	IMG_CAL086.170.fits	BIAS	****	-99	0.06
****	2	img_cal_bias	5	4	FORS1.2004-03-26T19:46:24.494.fits	IMG_CAL086.171.fits	BIAS	****	-99	0.06
****	2	img_cal_bias	5	5	FORS1.2004-03-26T19:47:08.608.fits	IMG_CAL086.172.fits	BIAS	****	-99	0.06
****	3	img_cal_bias	5	1	FORS1.2004-03-26T19:48:52.409.fits	IMG_CAL086.173.fits	BIAS	****	-99	0.06
****	3	img_cal_bias	5	2	FORS1.2004-03-26T19:49:36.773.fits	IMG_CAL086.174.fits	BIAS	****	-99	0.06
****	3	img_cal_bias	5	3	FORS1.2004-03-26T19:50:20.937.fits	IMG_CAL086.175.fits	BIAS	****	-99	0.06
****	3	img_cal_bias	5	4	FORS1.2004-03-26T19:51:05.382.fits	IMG_CAL086.176.fits	BIAS	****	-99	0.06
****	3	img_cal_bias	5	5	FORS1.2004-03-26T19:51:49.666.fits	IMG_CAL086.177.fits	BIAS	****	-99	0.06
****	4	img_cal_bias	5	1	FORS1.2004-03-26T19:56:29.472.fits	IMG_CAL086.178.fits	BIAS	****	-99	0.06
****	4	img_cal_bias	5	2	FORS1.2004-03-26T19:57:13.777.fits	IMG_CAL086.179.fits	BIAS	****	-99	0.06
****	4	img_cal_bias	5	3	FORS1.2004-03-26T19:57:58.101.fits	IMG_CAL086.180.fits	BIAS	****	-99	0.06
****	4	img_cal_bias	5	4	FORS1.2004-03-26T19:58:42.445.fits	IMG_CAL086.181.fits	BIAS	****	-99	0.06
****	4	img_cal_bias	5	5	FORS1.2004-03-26T19:59:26.760.fits	IMG_CAL086.182.fits	BIAS	****	-99	0.06
****	5	img_cal_bias	5	1	FORS1.2004-03-26T20:06:18.020.fits	IMG_CAL086.183.fits	BIAS	****	-99	0.06
****	5	img_cal_bias	5	2	FORS1.2004-03-26T20:07:02.255.fits	IMG_CAL086.184.fits	BIAS	****	-99	0.06
****	5	img_cal_bias	5	3	FORS1.2004-03-26T20:07:46.569.fits	IMG_CAL086.185.fits	BIAS	****	-99	0.06
****	5	img_cal_bias	5	4	FORS1.2004-03-26T20:08:30.834.fits	IMG_CAL086.186.fits	BIAS	****	-99	0.06
****	5	img_cal_bias	5	5	FORS1.2004-03-26T20:09:15.228.fits	IMG_CAL086.187.fits	BIAS	****	-99	0.06
****	6	img_cal_bias	5	1	FORS1.2004-03-26T20:15:35.996.fits	IMG_CAL086.188.fits	BIAS	****	-99	0.06
****	6	img_cal_bias	5	2	FORS1.2004-03-26T20:16:20.580.fits	IMG_CAL086.189.fits	BIAS	****	-99	0.06
****	6	img_cal_bias	5	3	FORS1.2004-03-26T20:17:04.904.fits	IMG_CAL086.190.fits	BIAS	****	-99	0.06
****	6	img_cal_bias	5	4	FORS1.2004-03-26T20:17:49.328.fits	IMG_CAL086.191.fits	BIAS	****	-99	0.06
****	6	img_cal_bias	5	5	FORS1.2004-03-26T20:18:33.813.fits	IMG_CAL086.192.fits	BIAS	****	-99	0.06
****	2	img_cal_bias	5	1	FORS1.2004-03-27T10:37:58.775.fits	IMG_CAL087.fits	BIAS	****	-99	0.06
****	2	img_cal_bias	5	2	FORS1.2004-03-27T10:38:45.229.fits	IMG_CAL087.1.fits	BIAS	****	-99	0.06
****	2	img_cal_bias	5	3	FORS1.2004-03-27T10:39:29.254.fits	IMG_CAL087.2.fits	BIAS	****	-99	0.06
****	2	img_cal_bias	5	4	FORS1.2004-03-27T10:40:13.418.fits	IMG_CAL087.3.fits	BIAS	****	-99	0.06
****	2	img_cal_bias	5	5	FORS1.2004-03-27T10:40:57.443.fits	IMG_CAL087.4.fits	BIAS	****	-99	0.06

C Extracts from the Memo on FORS1 "SKYFLATS"

We here briefly discuss the memo (Mignani and Petr–Gotzens, 2005) concerning FORS twilight sky images, often referred to as "SKYFLATS", collected over a period of 7 months in 2003-2004. Two important points can be extracted from Figs. 7 through 17 of that memo (for easy reference the relevant figures are reproduced here). The two points are central to the understanding of the calibration properties of FORS, and we shall here go through them in a little detail. As an example we choose to look at the R band figures (Figs. 14–15), but the conclusions are the same for all bands.

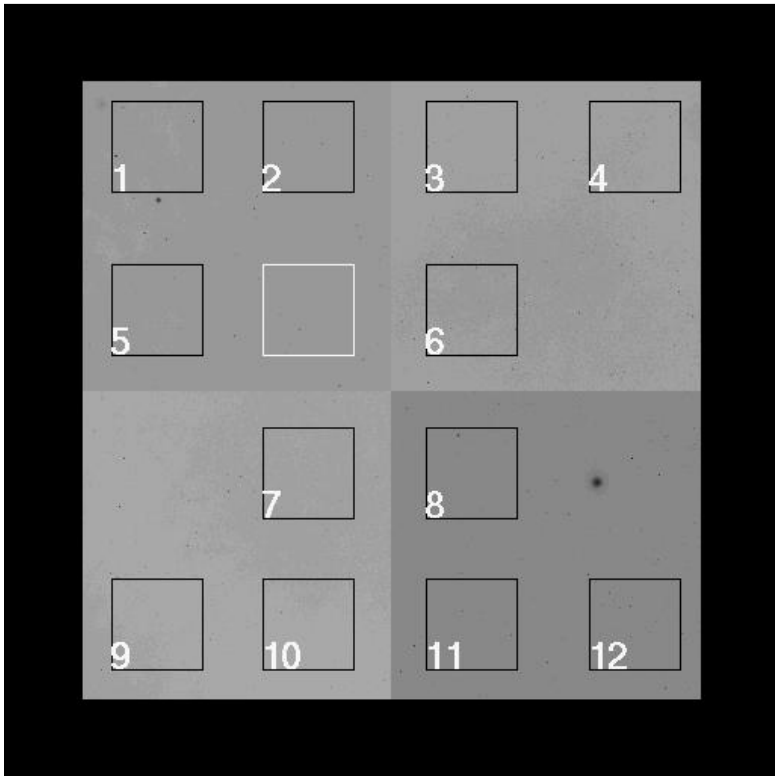

Figure 7: Position of the 12 test regions (black squares, numbered 1-12) and of the reference one (white square).

Fig. 14 shows the variation on large scales, as represented by the relative (normalized to unity) count level measured in 12 representative sub-frames, as defined in Fig. 7, over the CCD. It is seen that over some periods of up to 10 nights it is effectively constant, while at other times the night-to-night behaviour is seemingly completely erratic. Looking at each sub-frame in a bit more detail we see that the largest of the erratic jumps are found in sub-frames 9, 4, 12, and 1 (the 1σ's are 0.011, 0.010, 0.009 and 0.008). Those sub-frames represent the four corners of the CCD. The second largest variations are seen in sub-frames 10, 11, 3 and 2 (bottom and top parts of CCD), while the smallest 1σ's (0.003) are seen in the central sub-frames (5, 6, 7 and 8). The top-to-bottom variation is probably reflecting the actual variation of the gradient of the brightness of the

night sky. The strong variations in the corners look more like an instrumental effect, either variable vignetting or a variable scattered component. The total peak-to-peak variation over the 7 months is seen to be 0.977-1.029, i.e. 5.2%. Based on this we conclude that, if one uses the twilight sky images for flat fielding, one may likely introduce erratic zero-point variations across the field of up to 0.05-0.06 magnitude in R. The errors will be large in the corners, smaller towards the centre.

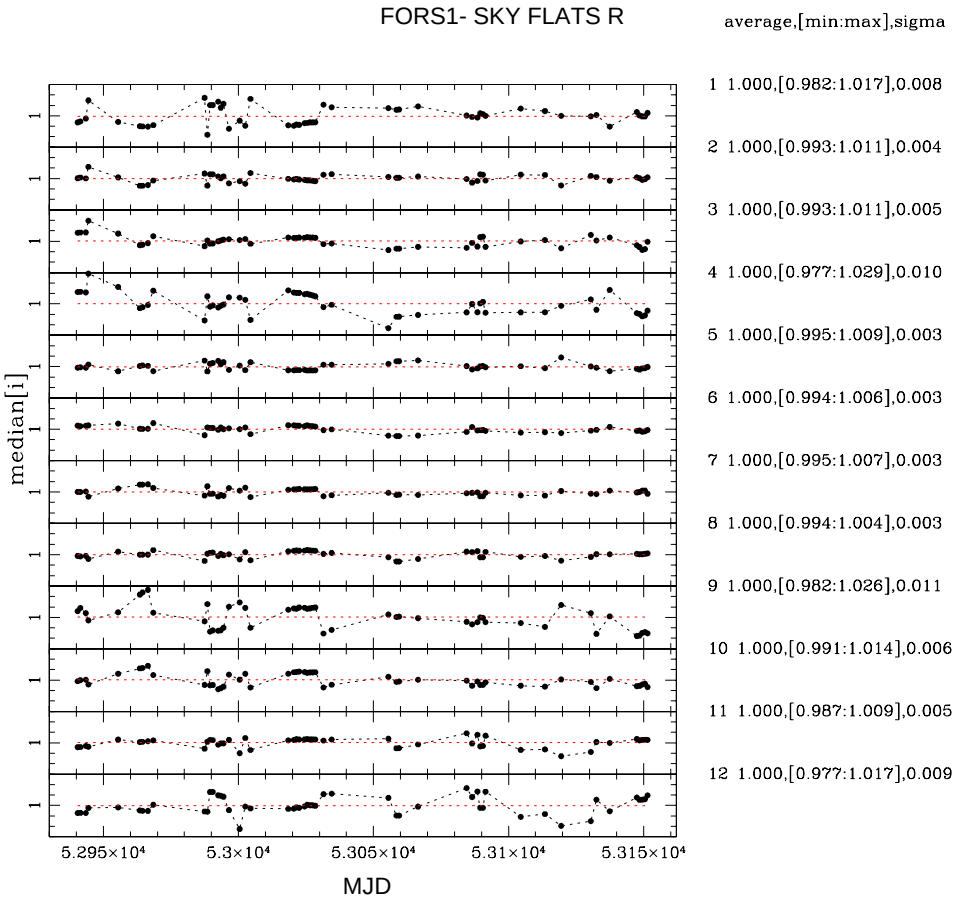

Figure 14: Same as Figure 8, but for the *R_BESS* filter.

Individual "master SKYFLATS" are combined from typically 4 twilight sky images each with roughly 25,000 counts. This implies that we expect rms's in the range 0.0024-0.0026. The size of the sub-frames (300 by 300 pixels) was selected hoping they would be small enough that a gradient across them would not dominate the rms measurement. However, a 5% variation across the CCD does correspond to an rms of 0.0024 measured over 300 pixels. Adding the expected variation and the random noise in square we get 0.0035 as the expected rms in the mean. From Fig. 15 we see that the measured rms shows no systematic increase over time, and that its level is in the range 0.0033-0.0039 in the 12 sub-frames. The rms measurements are therefore fully consistent with a constant pixel-to-pixel efficiency pattern, and we can set an upper limit to any time-evolution of about 0.002 per pixel, in the mean, over 7 months.

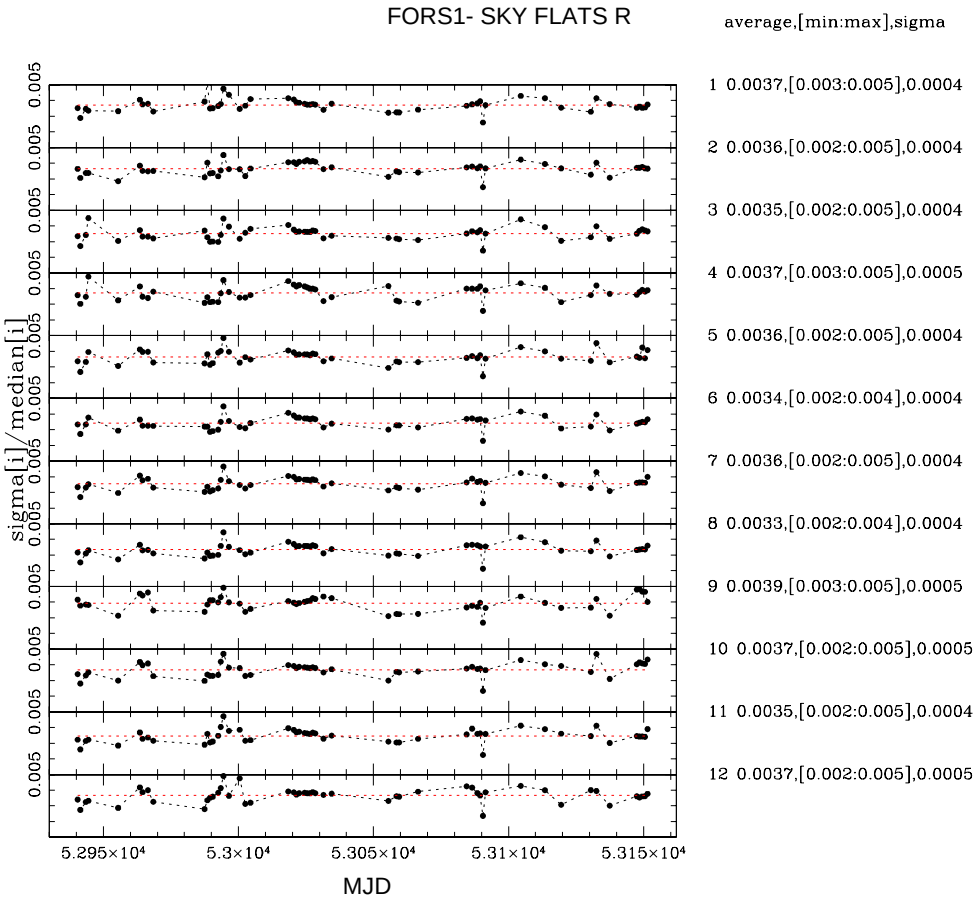

Figure 15: Same as Figure 9, but for the *R_BESS* filter.

D Atmospheric Intensity Scintillation

The atmospheric scintillation is often a problem for accurate photometry with small telescopes, but the problem becomes smaller for larger apertures. From Fig. 20 (adapted from Young, A. T., 1967; see also Dravins, D., Lindegren, L., Mezey, E., Young, A. T., 1998) we see that already at 1 second the scintillation is only 1.2 milli-mag, i.e. negligible compared to the shutter accuracy.

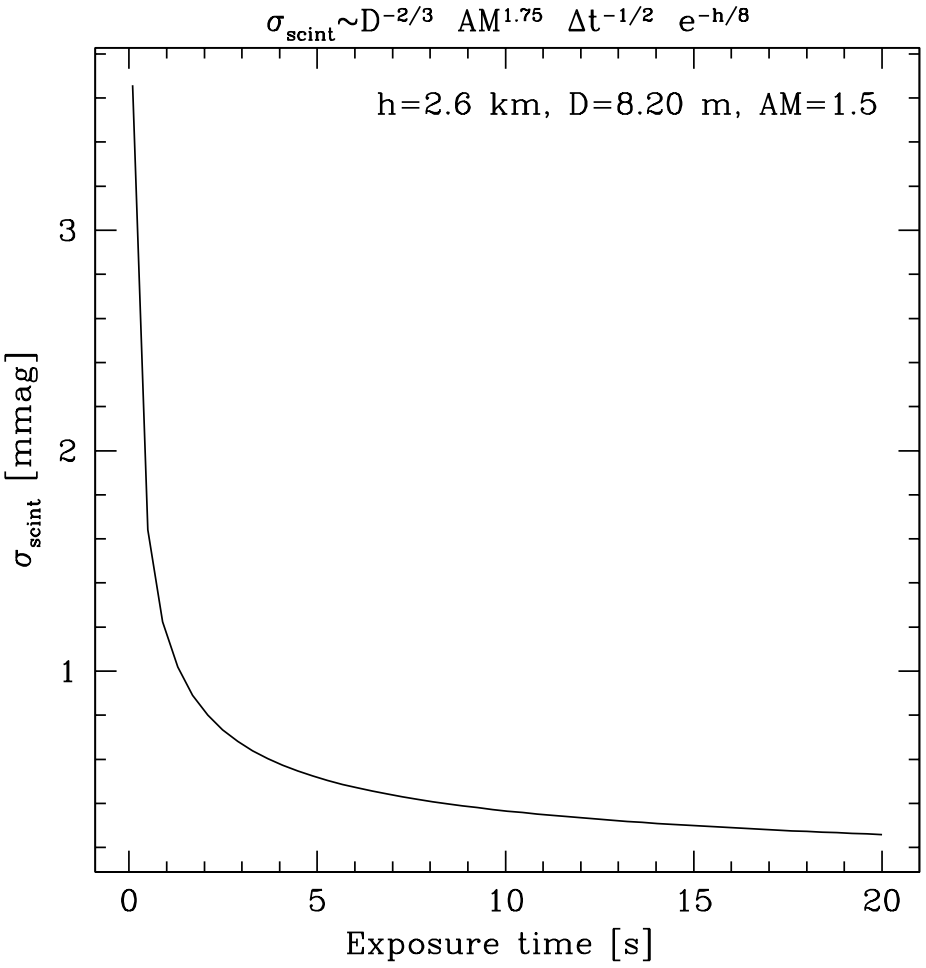

Figure 20: Atmospheric scintillation for a UT at airmass 1.5

E FSS-WG Report I

FORS IOT Secondary Standards Working Group – Report I:

FORS1 BIAS & Flatfield properties

A. Järvinen, P. Møller, M. Romaniello, F. Patat, W. Freudling, G. Rupprecht, M. V. D. Ancker, M. Petr-Gotzens, E. Jehin, R. Mignani, K. O'brien, T. Szeifert

2005-09-08

1 Introduction

This is the first of the two reports that will be delivered by the FISSWG. This report describes in detail the properties of the test data and the reduction steps taken in generating the master BIAS frame and master flatfields.

2 Data

The primary data set investigated included 160 BIAS frames, in total 8 B and 9 R twilight flatfields, and 13 B and 20 R standard star fields. All of the B flatfields were taken during the evening twilight. Two of the R flatfields were taken during the evening twilight and 7 during the morning twilight.

Of the standard star images, in B, we had 4 images without offsets with different rotation angles (180,90,0,-90), and 8 offset positions, in total 13 images of the field. All exposuretimes in B are 5 seconds.

In R band, we have 4 images without offsets with the same rotation angles as in B band and 4 offset positions with 2 to 3 images per position. For all positions there are 2 and 1 second exposures. The offset pattern used for B and R bands is given in Fig. 1.

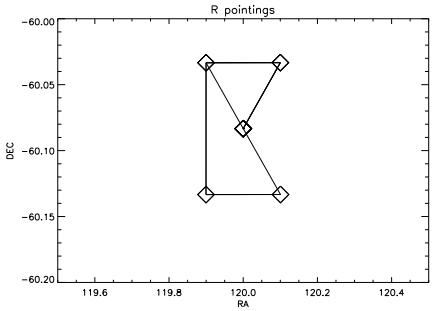

Figure 1: Pointing patterns for B and R band images.

3 BIASes

The FORS1 CCD (Tektronix TK2048EB4-1) is read out using four amplifiers and thus dividing the image into four quadrants. The quadrants are called A, B, C and D starting from lower left corner and counting anticlockwise. In order to study the stability and structure of the BIAS frames, a mean along columns (Y) was taken for plotting the profiles A–B and D–C and a mean along rows (X) was taken for plotting the profiles A–D and B–C. For crossprofile plots, the bottom and the top 100 rows and the left- and rightmost 16 columns, i.e. the overscan areas, were not used for calculating the mean values. In both cases sigma clipping with cut level at $\sigma = 4.5$ was used in order to remove cosmic events.

Fig. 2 illustrates that there are significant slopes in both directions in most of the quadrants; both horizontal and vertical in A and D and only horizontal in B and C. The BIAS levels do not settle to a constant value even close to the centre (i.e. even after reading out for a long time). Neither do the count levels come down to the level of the overscan areas. Also what can be seen is that the BIAS level ramps up in the first 100 rows in vertical plots and then turns downward not quite reaching the overscan level either.

The reason for the difference between overscan count level and the BIAS frame image area count level might be a (un)documented feature of FORS1 CCD/FIERA, but information on this could not be found from the instrument web pages. According to the quality-control department this offset and the slopes (ramping up/down) are common.

The slopes of the ramping up/down are on the level of 1 ADU over 1000 pixels (Fig. 3). For most quadrants the slopes are stable, but quadrant B shows some wiggling in the profile which varies with time, but the amplitude of the wiggling is below one ADU.

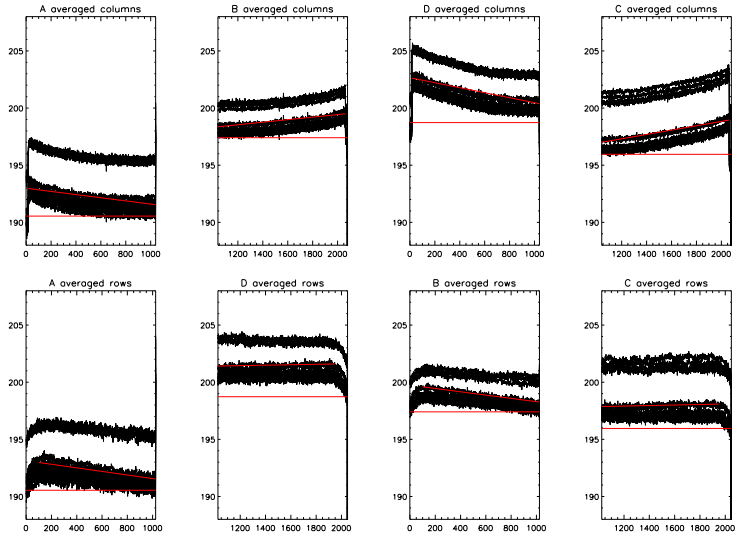

Figure 2: Crossprofiles averaged along columns (top) and rows (bottom).

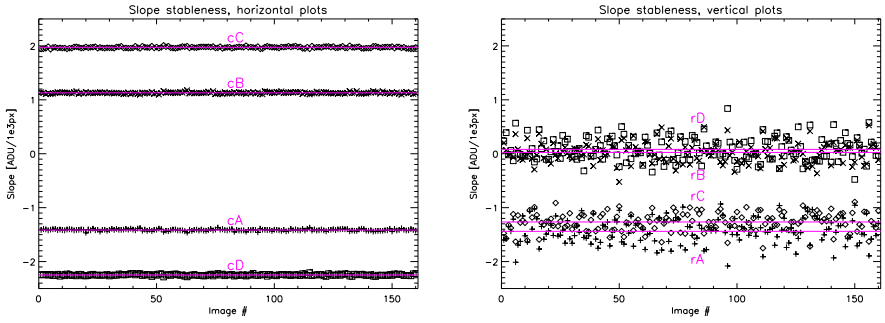

Figure 3: Slope coefficients for crossprofiles along columns (left) and along rows (right). Plot symbols for different quadrants are "+"=A, "X"=B, "◇"=C and "□"=D. Y-axis units are ADUs per 1000 pixels.

4 Procedure for BIAS subtraction

We investigated different methods for BIAS subtraction, and it was decided to proceed with 2-D BIAS subtraction in order to take the slopes into account. This was done by treating individual quadrants separately, and by creating a synthetic master BIAS by expanding the profiles in both horizontal and vertical directions. Procedure for BIAS subtraction is to first subtract the median of the overscan of the quadrant from the image to be processed and then subtract the synthetic BIAS frame.

The goodness of the synthetic BIAS frame was investigated by subtracting it from all of the individual BIAS frames. In the worst case the residuals from the subtraction are ± 0.27 ADUs. A crossprofile plot of one of the subtracted images is presented in Fig. 4.

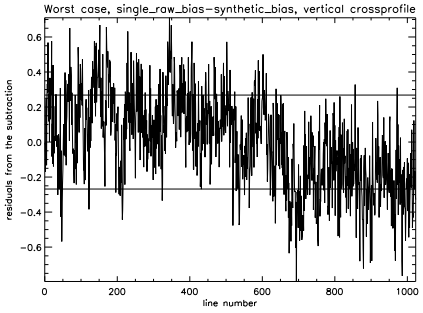

Figure 4: Worst case residuals of subtracting synthetic BIAS from individual BIAS frames, solid lines are plotted at 1σ rms.

The overscan areas were also inspected thoroughly. In case of FORS1 CCD, the overscan areas are not real pixels and, therefore, do not have exactly the same properties as the rest of the frame. The BIAS frames are normally obtained using templates consisting of 5 individual BIAS frame readouts. The overall overscan level changes linearly with time by 2-3 ADUs from the first frame of the template to the last (see Fig. 5). This might be an effect of temperature in the control electronics. In the 155 BIAS frames taken before the night this pattern was clearly seen inside each 5 frame template run. However, the offset between the overscan count level and the BIAS frame count level stays constant within the errors of the measurements.

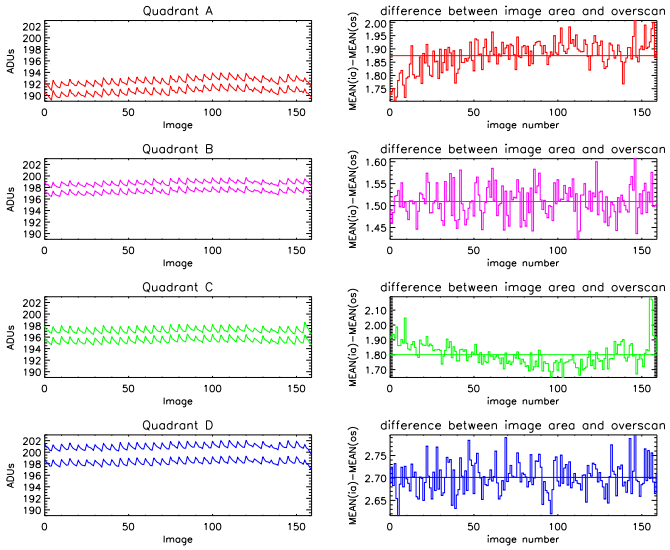

Figure 5: Count levels of the overscan areas of all of the frames (left) and the differences between the overscan and image area (right).

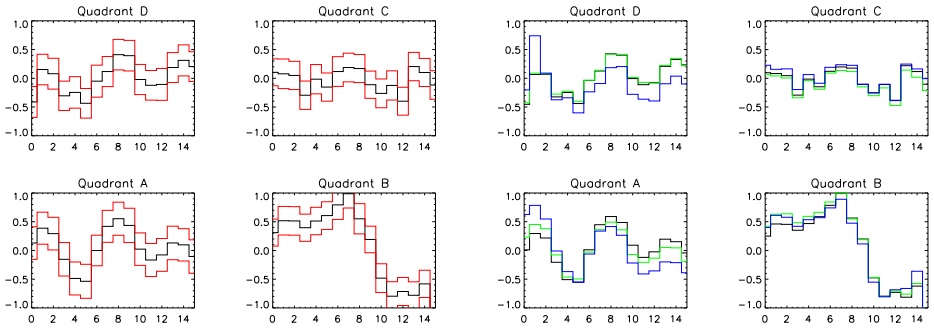

Figure 6: Overscan area profiles for each quadrant, left: combined for all 237 images (black line) with measured rms (red lines) right: separately for BIASes (black), flatfields (green) and standard star images (blue)

The crossprofile along the columns in the overscan areas has a distinct persistent pattern in each quadrant (see Fig. 6). This pattern is stable at least in timescales of days, and has a peak-to-peak amplitude of ~ 2 ADUs. The shape of the pattern has no dependence on the intensity level of the rest of the frame, but the overall count level has (see Fig. 7). This change is on

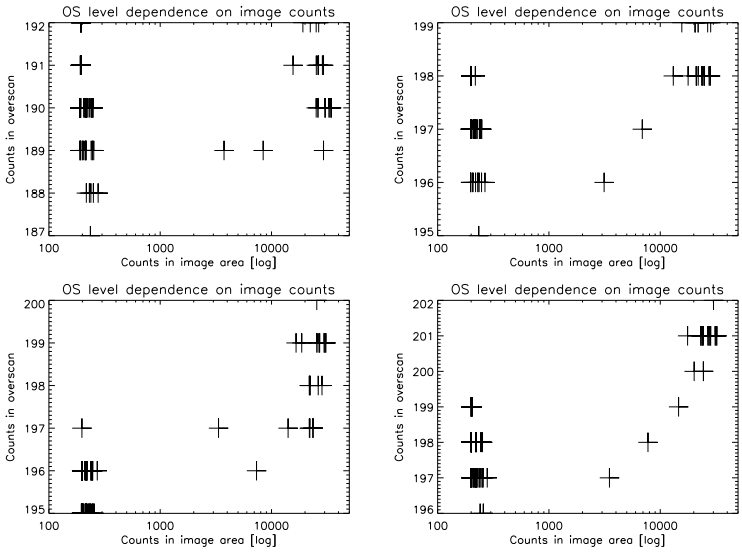

Figure 7: Differences in ADU levels between image area and overscan area in the BIAS frames.

the same level as inside BIAS frame template runs, and, therefore, does not cause extra concern. A wider overscan area might allow the CCD controller to settle, but it might also follow the pattern of the BIAS frame image area and not settle.

5 Bad Pixels

A bad pixel mask was generated for each individual flatfield frame by comparing each pixel value to its immediate surroundings and flagging out deviating high and low pixels. The results were combined, and if a pixel was found to deviate in all flat field images, it was marked as a bad pixel in the mask image.

The bad pixel mask was then used when combining the flatfields into a master flatfields for each filter. The masked pixels were not used in calculating the median in combining the flatfields. After median combining the individual quadrants, the master flatfield was "glued" back together, and normalised to 1.0 using statistics from the entire image area and all of the quadrants in order to retain the information of the different sensitivities of the individual CCD amplifiers of the different quadrants.

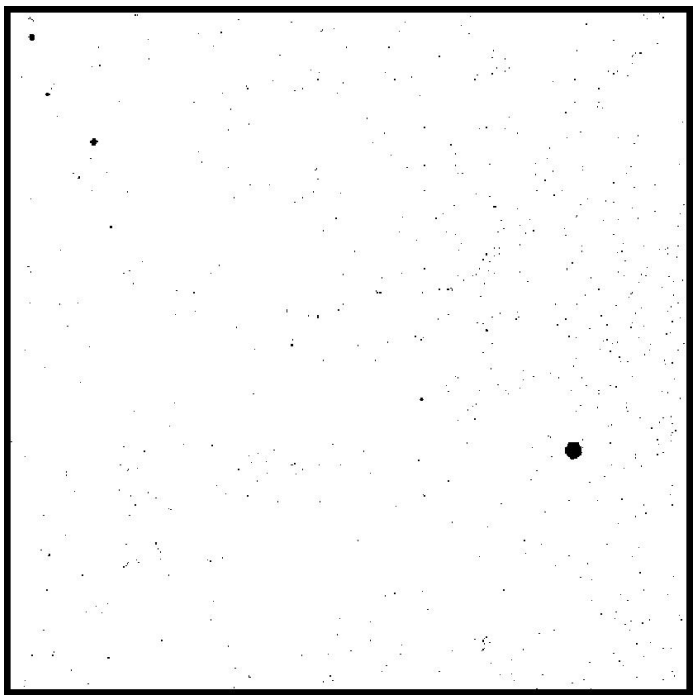

Figure 8: Bad pixel mask generated from B-band flatfields. Most notable feature is the "big black hole" in the B-quadrant. Black border added for clarity.

6 Flatfields

In the dataset obtained for this project, we had Bessel B and R band standard star data and, therefore, the efforts were concentrated on the respective twilight sky flatfield images. There was a concern that the overscan level would show different characteristics (ramping up or down) depending on the intensity level of the image area, but no indication of this was found. Only the mean count levels of the overscan areas increased in those flatfield frames which had high number of counts in the image area (see section 4 and Fig. 7).

The columns 17 and 2063 (i.e. the very first real physical pixels to be read out) were found to have significantly higher count levels than the rest of the image, and the top most row (2048, the very first row read out with amplifiers C and D) was found to have significantly lower count level in all flatfields. Experiment with dividing the first observed B flat with the last observed B flat resulted in a clear disagreement on the shape of the crossprofile on a level of 0.4% over the entire image area, peak-to-peak. For the R band the disagreement was 0.8%. These crossprofiles are presented in Fig. 9 and color-emphasised, smoothed R-band master twilight sky flatfield is shown in Fig. 11.

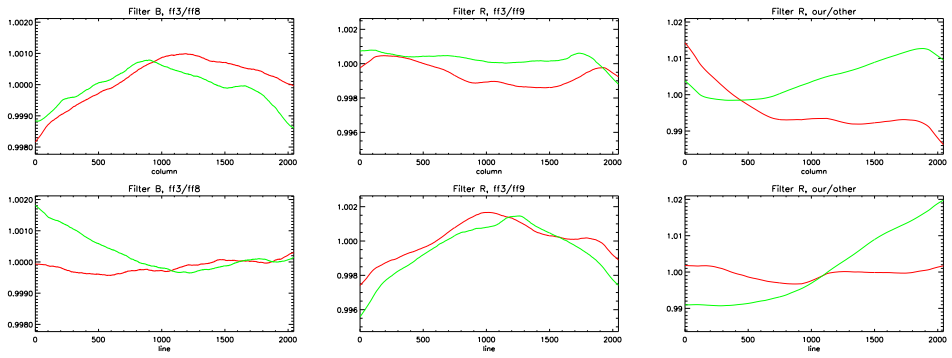

Figure 9: Crossprofiles of flatfields taken in the beginning of the evening twilight divided by last flatfields of the same twilight. From left to right: B band and R band of our dataset and R band flat of our set divided by R band flat from other dataset, taken 7 months later. Red and green line show the different two quadrants in both directions. In top plots red is A–B cut and in bottom plots A–D, similarly green line is D–C and B–C. The profiles have been boxcar smoothed using 201 pixel wide box, truncating box size at the edges.

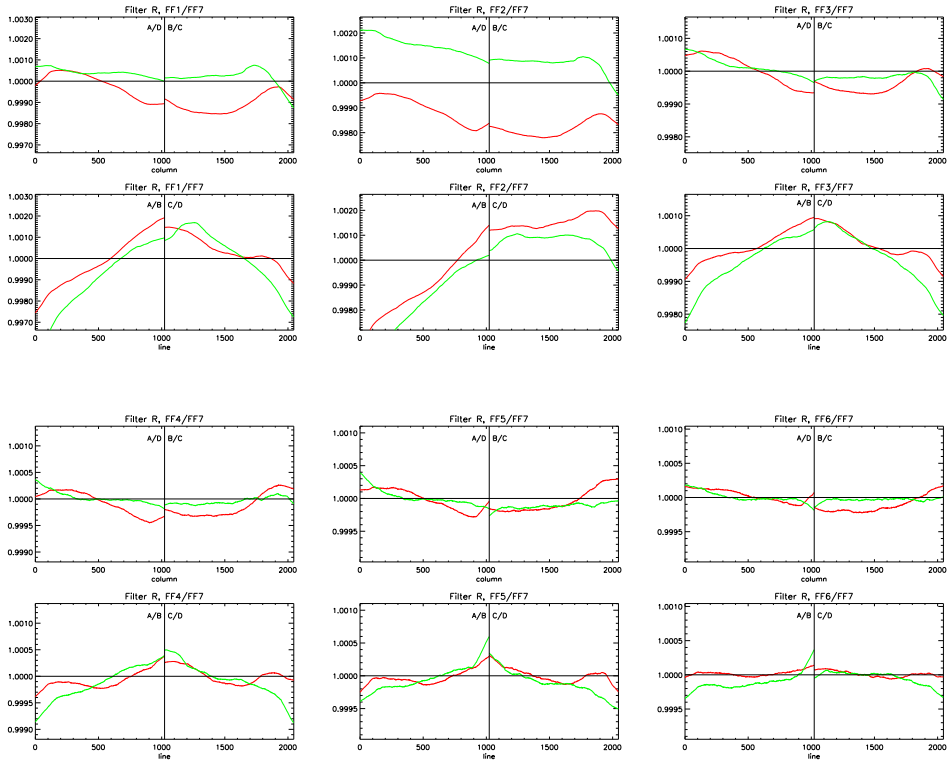

Figure 10: Crossprofiles of individual R band flatfields taken in the beginning of the morning twilight divided by the last morning twilight flatfield. Red and green line show the different two quadrants in both directions. In top plots red is A–B cut and in bottom plots A–D, similarly green line is D–C and B–C. The profiles have been boxcar smoothed using 201 pixel wide box, truncating box size at the edges.

In Technical Memo "Measure of the stability of the SKYFLATs in FORS1", it was found that the change in pixel to pixel variations is below 0.5% and does not vary much over 7 months time period, which includes this data set. Also found, was that the large scale structure in the flatfields varies significantly during the 7 months period. This we tested independently with the flatfields from this data set and with flatfields from another set of data taken for investigation by Wolfram et al. (see Fig. 9, right most pair). We found that there is a disagreement in the shapes of flatfield frames with peak-to-peak difference of 3%, which is significantly larger than that found inside same night Fig. 10.

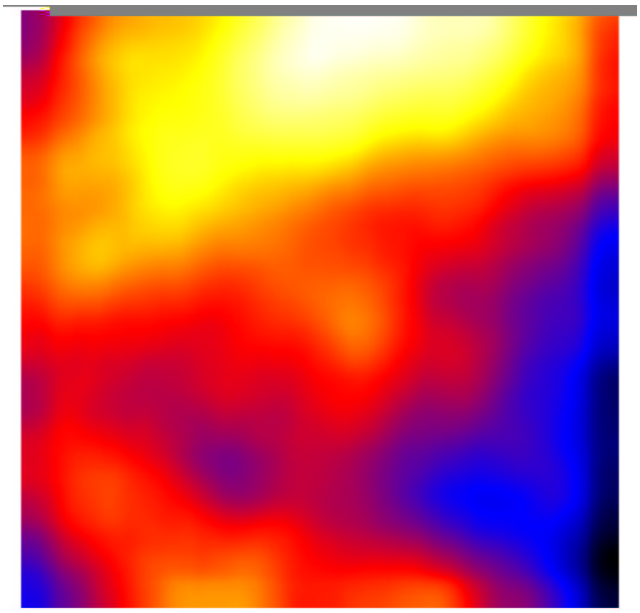

Figure 11: *R*-band twilight sky master flatfield frame, individual quadrants were first scaled to same mean and then the frame was smoothed with median filtering.

7 Conclusions

Outstanding conclusion is, that increasing the number of BIAS frames does not improve the photometry noticeably. Increasing the number of flatfield frames did not improve it either, mostly due to big variations from one flatfield to the other resulting in a systematic error of the order of 1% accross the field of view, peak-to-peak.

We experimented on the dataset using the methods presented in this report and comparing the resulting photometry with the same dataset reduced with the FORS1 pipeline, and found that there was no significant improvement over the currently used pipeline.

$$\_\_\_\_\ \Omega\ \_\_\_\_$$